Journal of Computational Electronics (2023) 22:310–332
https://doi.org/10.1007/s10825-022-01973-y

High-order accurate numerical simulation of monochromatic waves in photonic crystal ring resonators with the help of a non-iterative domain decomposition

Evan North[1] · **Semyon Tsynkov**[1] · **Eli Turkel**[2]

Received: 2 May 2022 / Accepted: 20 October 2022 / Published online: 20 November 2022

Abstract
A photonic crystal ring resonator (PCRR) is a micro-scale optical device that combines a closed-loop waveguide with a light input and output. PCRRs are constructed with periodically placed scattering rods where the exclusion of rods is used to form the path of a waveguide. We simulate PCRRs numerically using a non-iterative domain decomposition approach that is insensitive to jumps in material properties, in particular, those between the scattering rods and surrounding medium. To approximate the governing Helmholtz equation, we use a compact fourth-order accurate finite difference scheme combined with the method of difference potentials (MDP). The MDP renders exact coupling between the decomposition subdomains and maintains high-order accuracy for non-conforming boundaries/interfaces on regular grids.

Keywords Scattering rods · Periodic lattice · Helmholtz equation · Method of difference potentials · Exact coupling between non-overlapping subdomains · High-order accurate compact finite difference schemes

1 Introduction

A waveguide is a structure that allows the propagation only in a particular direction, such as sound passing through an instrument or air ducts. In optics, a ring resonator (Fig. 1a) is a closed-loop waveguide paired with a light input and output. The ring's geometry determines certain resonant frequencies that propagate from the input, around the ring, and out at the output. Because non-resonant frequencies will not propagate into and around the ring, the ring resonator acts as a filter where a range of frequencies is the input into the system, only allowing the resonant frequencies to propagate to the output channel.

✉ Semyon Tsynkov
tsynkov@math.ncsu.edu

Evan North
einorth@ncsu.edu

Eli Turkel
turkel@tauex.tau.ac.il

[1] Department of Mathematics, North Carolina State University, Box 8205, Raleigh, NC 27695, USA

[2] School of Mathematical Sciences, Tel Aviv University, 69978 Ramat Aviv, Tel Aviv, Israel

These resonators are used in a variety of optical applications, notably in fiber-optic cables. Recent applications are in the field of biosensing [1, 2], where ring resonators are integrated into micro-scale electronics, and an example of a dual-ring sensor is presented and analyzed in [3]. Unfortunately, such integrated waveguide ring resonators are known to suffer exponential propagation losses with the reduction of the ring radii. That sets a practical lower limit on the radius of the ring at a few micrometers [1], though work in [4, 5] suggests that the use of smart materials may be another way to alleviate this limitation.

For such micro-scale applications, photonic crystal ring resonators (PCRRs) offer a promising alternative, proving less sensitive to size-dependent losses [1]. PCRRs are constructed with periodically placed scattering rods where the exclusion of rods is used to form the path of the waveguide (e.g., Fig. 1b), with the rods themselves serving as a discrete alternative to a continuous wall. As a signal propagates through the waveguide, the rods refract and transmit the signal. This allows the signal to propagate down the open channels and into the central ring resonator in the usual fashion. Resonant frequencies can be tuned with the radius of the ring, as well as the size, material, and placement of the rods. Additionally, the periodic lattice of PCRRs can be structured with different symmetries (e.g., square, hexagonal,

octagonal, etc...) [6] depending on the application. A more advanced PCRR structure for a multifunctional logic gate is proposed and analyzed in [7] which explores certain nonlinear effects (Kerr nonlinearity) that arise as the structure (and applications) become more intricate.

Simulating the actual three-dimensional structure is costly, so two-dimensional simulations are commonly used as a surrogate for testing the efficacy of different arrangements of rods [1]. In the frequency domain, simulations involve solving the Helmholtz equation:

$$\Delta u + k^2 u = f$$

where k represents the wavenumber and is piecewise defined, representing the material properties of the background (typically air) or the rods individually. Due to the composite nature of the geometry of PCRRs, finite element methods have been the traditional solution method [8, 9]. These involve sophisticated grids with high refinement levels to accurately resolve the space around each rod, leading to costly simulations.

Alternatively, the structure of the PCRR suggests the use of a domain decomposition method (DDM), where each rod is handled in its own subdomain (see Fig. 2). Two known roadblocks for common iterative DDMs are cross-points (points where more than two subdomains meet) and discontinuous wavenumbers, both of which will be present in straightforward decompositions of a PCRR. Recent DDMs have found ways to mitigate these issues [10, 11], often through the use of context-dependent preconditioners or (computationally expensive) auxiliary variables. In our paper [12], we present a non-iterative DDM that is inherently insensitive to both cross-points and discontinuous wavenumbers. This insensitivity is due to the underlying use of the method of difference potentials (MDP) [13].

Rather than iteratively updating and matching boundary data along the interfaces, our method solves for all of the boundary and interface data simultaneously. The MDP benefits from the speed and convenience of a high-order finite difference method built on a regular, structured grid, even in the case of non-conforming geometries (such as the circular rods). Additionally, the MDP utilizes pre-computed operators that are built for a particular domain and unique for a given wavenumber. After the operators have been computed once they can simply be reused with new source or boundary data, assuming the geometry and wavenumber remain the same. In the context of DDMs, this property allows the same operators to be used for subproblems with the same shape and wavenumber. Our proposed decomposition of a PCRR only involves two kinds of subdomains—an empty square and a square with a rod, see Fig. 2. By computing only two sets of operators, we obtain the pre-computed information for hundreds of subdomains for free.

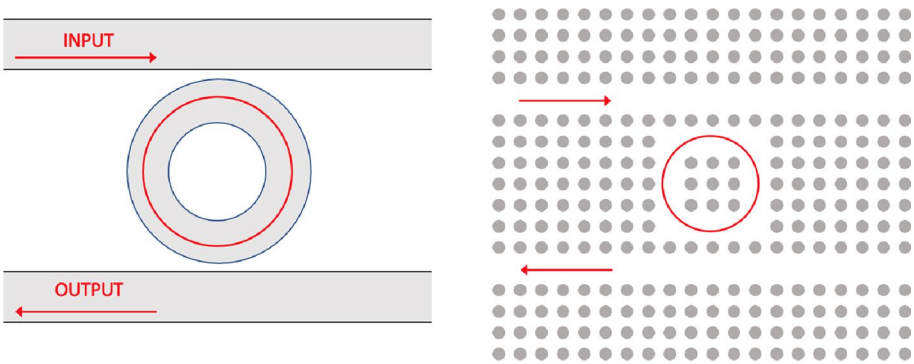

(a) Traditional ring Resonator **(b)** Photonic crystal ring resonator.

Fig. 1 Examples of ring resonator waveguides

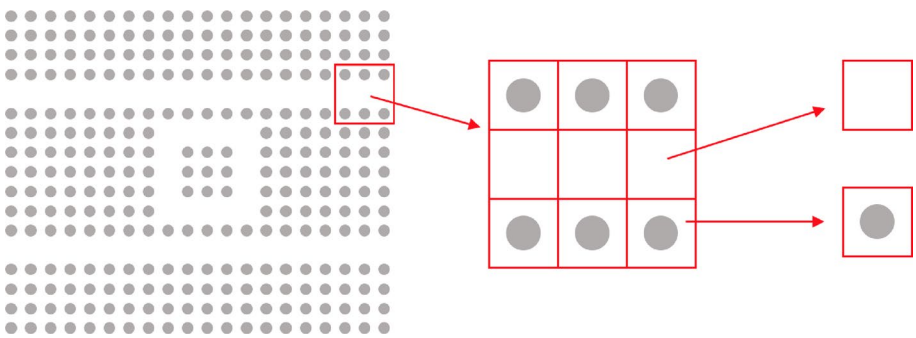

Fig. 2 Depiction of how a PCRR is built from a small set of basic subdomains (building blocks)

Summary of methods and results

In this work, we have developed, implemented and tested an efficient numerical method for simulating the monochromatic waves in PCRRs with high-order accuracy. Its key advantage is the capacity to easily modify the structure of the resonator, which is achieved by having a large-scale numerical model assembled from duplicates of a small number of distinct elements that are pre-computed ahead of time. This is enabled by a non-iterative domain decomposition technique that we have previously constructed [12]. Our domain decomposition technique employs the method of difference potentials [14].

Outline of the paper

Section 2 provides a review of the various components used in our method: Absorbing boundary conditions, domain decomposition, and a fourth-order finite difference method. Section 3 briefly explains how to construct the auxiliary problems and operators (difference potentials and extension) that incorporate the scattering rods. In Sect. 3.3 specifically, we review the construction of the core linear system and explain how to resolve interface and absorbing boundary conditions. Section 4 provides two kinds of numerical results: error analysis (Sect. 4.1) and PCRR simulations (Sect. 4.2). Finally, in Sect. 5 we summarize the current developments and propose directions for future work.

2 Preliminaries

Consider the Helmholtz equation over a domain $\Omega \subset \mathbb{R}^2$ with boundary $\partial\Omega$:

$$\Delta u + k^2 u = f, \quad \text{in } \Omega \tag{1a}$$

$$\mathcal{B}u = \phi, \quad \text{on } \partial\Omega \tag{1b}$$

where the operator $\mathcal{B}$ defines the boundary condition given on $\partial\Omega$. It is well-known that solving () numerically is prone to many potential difficulties: possible non-uniqueness (resonances), artificial reflections from outgoing waves, loss of regularity at material interfaces, and the pollution effect [15, 16], to name a few.

In this section, we provide a brief introduction to several components of our method that address our approach to the difficulties listed above. In Sect. 2.1, we address the choice of absorbing boundary conditions which permit simulated waves to propagate outward toward infinity. Section 2.2 introduces the fundamental terminology, notation, and concepts that we use for the domain decomposition. Finally, in Sect. 2.3 we present and justify the finite difference method that provides the underlying discretization on the grid.

2.1 Absorbing boundary conditions

When simulating a PCRR, waves continue propagating toward infinity when they leave the domain of interest, contributing no reflections back into the domain of interest. Traditionally, this effect is modeled by the Sommerfeld radiation condition [17]

$$\lim_{r\to\infty} \sqrt{r}\Big(\frac{\partial}{\partial r} - ik\Big)u(x,y) = 0 \tag{2}$$

where $r = \sqrt{x^2+y^2}$. This exact boundary condition is imposed at infinity, making it ill-suited for use in computational methods. Instead, we introduce an approximation of (2) called an *absorbing boundary condition* (ABC) at the edge of the domain. The simplest example of such an ABC is obtained by enforcing (2) on the boundary of the domain (rather than at infinity):

$$\Big(\frac{\partial}{\partial \mathbf{n}} - ik\Big)u = 0, \quad \text{on } \partial\Omega$$

where $\mathbf{n}$ represents the outward normal direction with respect to $\partial\Omega$. By its nature as an approximation, an ABC is inexact and will produce artificial reflections at the boundary which travel back into the domain of interest. A better quality ABC generates fewer reflections.

Various approaches have been taken to produce ABCs that reduce the artificial reflections, see approaches by Engquist and Majda [18], Hagstrom and Hariharan [19], and Bayliss et al. [20, 21] (see [22] for a cohesive review of these and other methods). Under certain conditions, several of these conditions have been shown to be equivalent, making the appropriate choice highly context-dependent. We consider the second-order ABC developed by Engquist and Majda [18]:

$$\mathcal{B}u \overset{\text{def}}{=} ik\frac{\partial u}{\partial \mathbf{n}} - k^2 u - \frac{1}{2}\frac{\partial^2 u}{\partial \tau^2} = 0 \tag{3}$$

where $\frac{\partial}{\partial \tau}$ represents differentiation with respect to the tangential coordinate. The normal and tangential coordinates used in (3) conveniently translate into Cartesian coordinates when the condition is set on the edge of a square, unlike the polar coordinates used to derive many other ABCs. Details of how we implement (3) within our method can be found in Sect. 3.3.1.

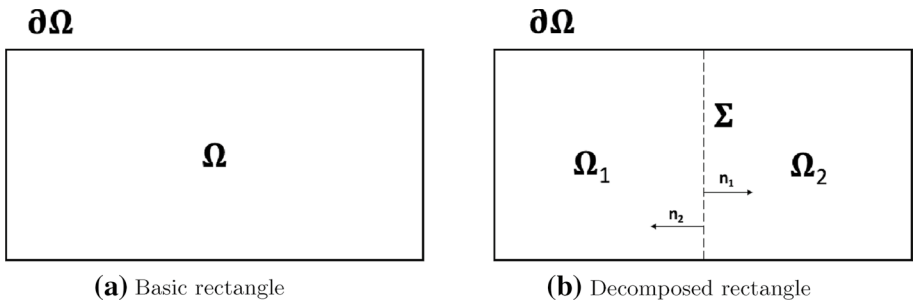

(a) Basic rectangle **(b)** Decomposed rectangle

Fig. 3 The interface Σ is introduced to split Ω into two subdomains, Ω_1 and Ω_2. The vectors $\mathbf{n}_1, \mathbf{n}_2$ denote the outward normal direction along Σ for Ω_1 and Ω_2, respectively

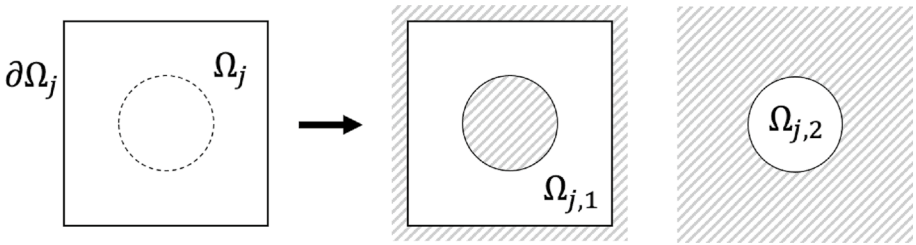

Fig. 4 Decomposition of the rod subdomain into two of its own subdomains such that $\Omega_j = \Omega_{j,1} \cup \overline{\Omega}_{j,2}$. The dotted circle is not part of $\partial\Omega_j$

2.2 Decomposition formulation

The decomposition of the PCRR relies on two fundamental building blocks: an empty square and a square that contains a circle (Fig. 2). The empty square building block can be visualized in Fig. 3, where a larger (rectangular) domain Ω is split into two identical subdomains Ω_1 and Ω_2 by an interface Σ. The formulation of the Helmholtz BVP () can then be expressed as

$$\begin{cases} \Delta u_1 + k_1^2 u_1 = f, & \text{in } \Omega_1 \\ \mathcal{B} u_1 = \phi, & \text{on } \overline{\Omega}_1 \cap \partial\Omega \end{cases} \quad \begin{cases} \Delta u_2 + k_2^2 u_2 = f, & \text{in } \Omega_2 \\ \mathcal{B} u_2 = \phi, & \text{on } \overline{\Omega}_2 \cap \partial\Omega \end{cases} \tag{4a}$$

$$\begin{cases} u_1 = u_2, & \text{on } \Sigma \\ \frac{\partial u_1}{\partial \mathbf{n}_1} = -\frac{\partial u_2}{\partial \mathbf{n}_2}, & \text{on } \Sigma \end{cases} \tag{4b}$$

where the wavenumbers k_1 and k_2 characterize the material properties in Ω_1 and Ω_2, respectively. Note that subproblems (4a) only have boundary conditions defined along their exterior edges, leaving them underdetermined. The two conditions of (4b) provide the necessary conditions along the interface Σ to ensure the solution of () on each subdomain matches that of (), i.e.,

$$\begin{cases} u = u_1 \text{ in } \Omega_1 \\ u = u_2 \text{ in } \Omega_2 \end{cases}$$

Although other transmission conditions can be used in place of (4b), we note that the solutions obtained in the respective subdomains would no longer match their corresponding parts of the global solution to ().

The second building block, the square that contains a circle (henceforth referred to as the "rod subdomain") is itself treated as a decomposition into two pieces: the circle itself and the rest of the square outside of the circle (see Fig. 4). In this decomposition, the interface Σ is the circle.

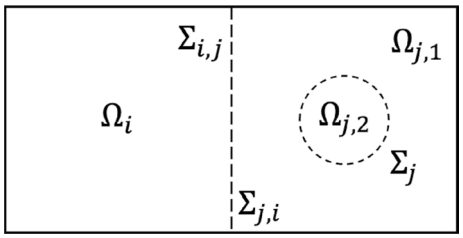

Fig. 5 Example of how various parts of a composite domain are labeled when considered as part of the same decomposition

Physically, the rod subdomain is used to model parts of the PCRR where the scattering rods exist and create material discontinuities. Therefore, when reformulating () over the rod subdomain Ω_j we allow k to change as it crosses the circle, i.e.,

$$\begin{cases} \Delta u_1 + k_1^2 u_1 = f & \text{in } \Omega_{j,1} \\ \mathcal{B} u_1 = \phi & \text{on } \partial\Omega_j \end{cases} \tag{5a}$$

$$\{ \Delta u_2 + k_2^2 u_2 = 0 \text{ in } \Omega_{j,2} \tag{5b}$$

$$\begin{cases} u_1 = u_2, & \text{on } \overline{\Omega}_{j,1} \cap \overline{\Omega}_{j,2} \\ \frac{\partial u_1}{\partial \mathbf{n}_1} = -\frac{\partial u_2}{\partial \mathbf{n}_2}, & \text{on } \overline{\Omega}_{j,1} \cap \overline{\Omega}_{j,2} \end{cases} \tag{5c}$$

Note that, the subproblem (5b) does not have a boundary condition explicitly associated with it, and that the entirety of the boundary condition (1b) is associated with (5a).

Instead, the boundary information for (5b) is provided solely by the transmission conditions (5c). If $k_1 = k_2$, this subproblem becomes mathematically equivalent to the empty subdomain case [12], so we generally assume $k_1 \neq k_2$.

For decompositions that incorporate both kinds of subdomains, we follow the notation introduced in Fig. 5. Interfaces between two separate squares Ω_i and Ω_j are labeled $\Sigma_{i,j}$. Thus, $\Sigma_{i,j}$ and $\Sigma_{j,i}$ are equivalent and can be used interchangeably. Within a rod subdomain Ω_j, the circular interface is simply denoted Σ_j. The decomposition of Ω_j remains consistent with Fig. 4, where $\Omega_j = \Omega_{j,1} \cup \overline{\Omega}_{j,2}$.

2.3 Finite difference scheme

The MDP can be implemented in conjunction with any finite difference scheme as the underlying approximation, even in the case of complex or non-conforming boundaries. High-order schemes are effective in combating the well-known pollution effect [16, 23, 24], generally achieving higher accuracy with coarser discretizations. Compact schemes do not require additional boundary conditions beyond those supplied with the differential equation itself. Therefore, we have chosen to use the fourth-order, compact scheme for the Helmholtz equation as presented in [25, 26]

$$\begin{aligned}
&\frac{1}{h^2}\left(u_{m+1,n} + u_{m-1,n} + u_{m,n+1} + u_{m,n-1} - 4u_{m,n}\right) \\
&\quad + \frac{1}{6h^2}\left[u_{m+1,n+1} + u_{m-1,n+1} + u_{m+1,n-1}\right. \\
&\quad + u_{m-1,n-1} + 4u_{m,n} \\
&\quad \left. - 2\left(u_{m+1,n} + u_{m-1,n} + u_{m,n+1} + u_{m,n-1}\right)\right] \\
&\quad + \frac{k^2}{12}\left(u_{m+1,n} + u_{m-1,n} + u_{m,n+1}\right. \\
&\quad \left. + u_{m,n-1} + 8u_{m,n}\right) \\
&= f_{m,n} + \frac{1}{12}\left(f_{m+1,n} + f_{m-1,n}\right. \\
&\quad \left. + f_{m,n+1} + f_{m,n-1} - 4f_{m,n}\right)
\end{aligned} \tag{6}$$

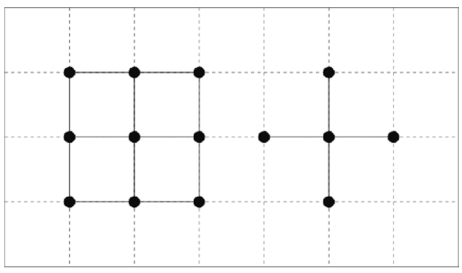

Fig. 6 The stencils for the compact scheme given in (6)

The scheme (6) uses a 9-point stencil for the left-hand side of the PDE and a 5-point stencil for the right-hand side (see Fig. 6) with uniform step size in the $x-$ and $y-$ directions ($\Delta x = \Delta y = h$). Additionally, (6) was derived with the assumption of a constant wavenumber, k. This assumption suffices for us because we assume that the decomposition yields subdomains that each have their own constant value of k. One could also consider a sixth-order scheme for constant [27] or variable [28] wavenumber, or a fourth-order scheme for a more general form of the Helmholtz equation with a variable coefficient Laplace-like term and wavenumber [29]. However, for the scope of this paper we will focus on the case of piecewise constant k.

3 Method of difference potentials

In this section, we introduce the method of difference potentials in the context of the rod subdomain. The individual pieces of the formulation have been more rigorously introduced and explored in previous works [13, 30–35], and the case of the empty subdomain is covered in [12]. Our intention with this section is to present these individual pieces within a unified framework as they relate to the decomposition of the PCRR. The following sections are intended to only provide the definitions relevant to the current paper. Many of the equations and definitions are direct extensions of the work in [12] and are presented here without discussion or justification. Refer to [12] and the citations therewithin for a more complete presentation of the material.

3.1 Auxiliary problems

Computing the Calderon's potentials and projections requires setting an appropriate auxiliary problem (AP), which serves to define an inverse to the discrete Helmholtz operator. The AP is formulated on an auxiliary domain that contains the physical domain as a subset. It should be uniquely solvable and well-posed, and should admit an efficient numerical solution. Otherwise, the AP can be arbitrary [13] and our specific choice is made for the reason of convenience. We start by briefly introducing the auxiliary problem for the empty subdomain [12] to show how the same AP can be used for part of the rod subdomain that is exterior to the circle ($\Omega_{j,1}$ in Fig. 4). Additionally, we introduce an AP for the interior of the circle in the rod subdomain.

Let Ω_j be a square with side length $2L$, centered about the origin. Define the auxiliary domain $\Omega^{0,\epsilon_1} \supset \Omega_j$ to be the square of side length $2(L + \varepsilon_1)$ for some small $\varepsilon_1 > 0$ (Fig. 7, practical choices for ϵ_1 are discussed in Sect. 4). Consider the following auxiliary problem:

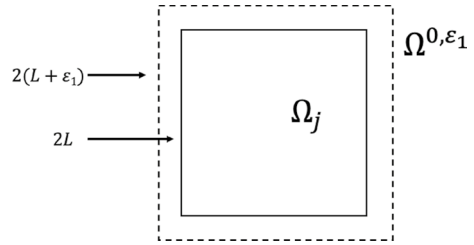

Fig. 7 Auxiliary domain Ω^0 surrounding an empty subdomain Ω_j

$$\begin{cases} \mathcal{L}_j u \equiv (\Delta + k_j^2)u = g & (x,y) \in \Omega^{0,\varepsilon_1} \\ u = 0 & y = \pm(L+\varepsilon_1) \\ \frac{\partial u}{\partial x} + ik_j u = 0 & x = L+\varepsilon_1 \\ \frac{\partial u}{\partial x} - ik_j u = 0 & x = -L-\varepsilon_1 \end{cases} \tag{7}$$

The AP (7) is defined for any right-hand side (RHS) g. The Sommerfeld-like conditions on x–bounds are chosen to ensure the AP is well-posed by shifting the spectrum of the subproblem to the complex plane, ensuring resonance is avoided for any real wavenumber k_j. The Dirichlet conditions on y–bounds permit an efficient numerical solution by means of a sine-FFT in y–direction paired with a tridiagonal solver.

Let Ω_j be a rod subdomain (Fig. 4) such that the boundary $\partial\Omega_j$ is again a square with side length $2L$ and is centered about the origin, and let the circle inside the rod subdomain $\Omega_{j,2}$ have radius R. Further, let the material discontinuity be characterized by the following definition of the wavenumber k_j:

$$k_j = \begin{cases} k_{j,1} & (x,y) \in \Omega_{j,1} \\ k_{j,2} & (x,y) \in \Omega_{j,2} \end{cases}$$

The rod subdomain requires the definition of two auxiliary problems. The first of these APs is equivalent to (7) and accounts for the solution inside of $\Omega_{j,1}$. Note that even though k_j has a discontinuity, this AP still uses the constant value assigned to $\Omega_{j,1}$, i.e.,

$$\begin{cases} \mathcal{L}_{j,1} u \equiv \Delta u + k_{j,1}^2 u = g & (x,y) \in \Omega^{0,\varepsilon_1} \\ u = 0 & y = \pm(L+\varepsilon_1) \\ \frac{\partial u}{\partial x} + ik_{j,1} u = 0 & x = L+\varepsilon_1 \\ \frac{\partial u}{\partial x} - ik_{j,1} u = 0 & x = -L-\varepsilon_1 \end{cases} \tag{8a}$$

The second AP handles the interior of the circle and requires its own auxiliary domain. Let $\varepsilon_2 > 0$ be given and define Ω^{0,ε_2} to be a square of side length $2(R+\varepsilon_2)$ so that $\Omega^{0,\varepsilon_2} \supset \Omega_{j,2}$. The second AP is formulated on Ω^{0,ε_2}:

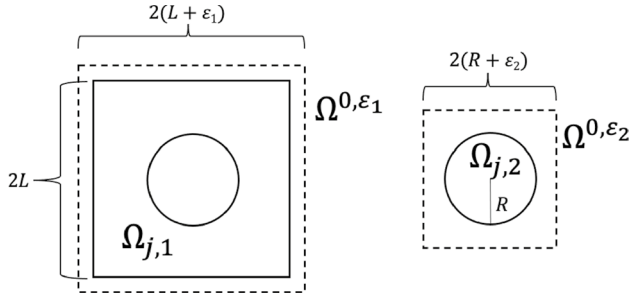

Fig. 8 Auxiliary domains Ω^{0,ε_1} and Ω^{0,ε_2} depicted containing their respective domains. Ω_j can be an empty or rod subdomain

$$\begin{cases} \mathcal{L}_{j,2} u \equiv \Delta u + k_{j,2}^2 u = g & (x,y) \in \Omega^{0,\varepsilon_2} \\ u = 0 & y = \pm(R+\varepsilon_2) \\ \frac{\partial u}{\partial x} + ik_{j,2} u = 0 & x = R+\varepsilon_2 \\ \frac{\partial u}{\partial x} - ik_{j,2} u = 0 & x = -R-\varepsilon_2 \end{cases} \tag{8b}$$

Figure 8 depicts both auxiliary domains, Ω^{0,ε_1} and Ω^{0,ε_2} in relation to their respective subdomains. The Helmholtz operators $\mathcal{L}_{j,1} = (\Delta + k_{j,1}^2)$ and $\mathcal{L}_{j,2} = (\Delta + k_{j,2}^2)$ of the rod subdomain APs (8a) and (8b) are discretized using the left-hand side of the finite difference scheme (6) with the discrete counterparts denoted by $\mathcal{L}_{j,1}^{(h)}$ and $\mathcal{L}_{j,2}^{(h)}$, respectively. In order to preserve the overall accuracy of the scheme, the boundary conditions from the APs also need to be discretized to fourth-order. The Dirichlet conditions on y–bounds are trivial as the boundary nodes simply are set to zero, i.e., for a discretization with $M+1$ nodes in the x–direction and $N+1$ nodes in the y–direction, set

$$u_{m,0} = u_{m,N} = 0, \qquad m = 0, ..., M \tag{9a}$$

For the conditions on the x–bounds, we use the following discretization, derived for the variable coefficient Helmholtz equation in [29] and simplified for the constant-coefficient case in [35]:

$$\begin{aligned} &\Big(\frac{u_{M,n} - u_{M-1,n}}{h} \\ &\quad - \frac{1}{6h}\big(u_{M,n+1} - u_{M-1,n+1} + u_{M,n-1} - u_{M-1,n-1} \\ &\quad -2\big(u_{M,n} - u_{M-1,n}\big)\big) \\ &\quad - \frac{k^2 h}{24}\big(u_{M,n} - u_{M-1,n}\big)\Big) \\ &\quad + ik\Big(\frac{u_{M,n} - u_{M-1,n}}{h} + \frac{h^2 k^2}{8} u_{M-\frac{1}{2},n} \\ &\quad + \frac{u_{M-\frac{1}{2},n+1} - 2u_{M-\frac{1}{2},n} + u_{M-\frac{1}{2},n-1}}{2} \Big) = 0 \end{aligned} \tag{9b}$$

$$\Big(\frac{u_{1,n}-u_{0,n}}{h} - \frac{1}{6h}\big(u_{1,n+1}-u_{0,n+1}+u_{1,n-1}-u_{0,n-1}-2\big(u_{1,n}-u_{0,n}\big)\big) - \frac{k^2h}{24}\big(u_{1,n}-u_{0,n}\big)\Big) - ik\Big(\frac{u_{1,n}-u_{0,n}}{h} + \frac{h^2k^2}{8}u_{\frac{1}{2},n} + \frac{u_{\frac{1}{2},n+1}-2u_{\frac{1}{2},n}+u_{\frac{1}{2},n-1}}{2}\Big) = 0. \tag{9c}$$

The discrete APs for the rod subdomain can now be expressed as $\mathcal{L}^{(h)}_{j,1}u^{(h)} = g^{(h)}$ and $\mathcal{L}^{(h)}_{j,2}u^{(h)} = g^{(h)}$, subject to the discrete boundary conditions (). Since (8a) and (7) are basically the same, $\mathcal{L}^{(h)}_{j,1}u^{(h)} = g^{(h)}$ also discretizes (7). Like their continuous counterparts () (and (7)), the discrete APs have unique solutions for any right-hand side $g^{(h)}$. Indeed, each of these APs can be solved directly by a combination of the FFT in the y direction and tridiagonal elimination in the x direction. The resulting solutions define the inverse operators $\mathcal{G}^{(h)}_{j,l}$: $u^{(h)} = \mathcal{G}^{(h)}_{j,l}g^{(h)}$ for $l = 1, 2$. By design, the operators $\mathcal{G}^{(h)}_{j,l}$ apply to an arbitrary $g^{(h)}$. If f represents a physical source function, see equation (1a), then

$$g^{(h)} = \mathcal{B}^{(h)}f \overset{\text{def}}{=} f_{m,n} + \frac{1}{12}\big(f_{m+1,n} + f_{m-1,n} + f_{m,n+1} + f_{m,n-1} - 4f_{m,n}\big) \tag{10}$$

where $\mathcal{B}^{(h)}$ denotes the application of the right-hand side stencil from (6). However, for constructing the difference potentials the operators $\mathcal{G}^{(h)}_{j,l}$ will need to be applied to the right-hand sides $g^{(h)}$ other than (10) as well, see Sects. 3.2 and 3.3.

3.2 Difference potentials and operators

In this section, we start by defining the grid sets that serve as discrete analogs for the various parts of the rod subdomain. These grid sets are used to define the difference potential, which is the key operator and discrete analog to the Calderon's operator. The difference potential in turn defines the boundary projection operator. Following the example of [12, 31, 35], we also present the equation-based extension operator that links the continuous data to the discrete nodes as well as the spectral representation of the solution at the boundary. Throughout this section, we are only considering a single rod subdomain Ω_j. As such, the subscript indices are simplified and restricted to $l \in \{1, 2\}$ to indicate whether the grid set or operator is constructed for $\Omega_{j,1}$ or $\Omega_{j,2}$, dropping the first index j altogether.

Let $\mathbb{N}^0_l$ be a uniformly spaced Cartesian grid over Ω^{0,ε_l} and $\mathbb{M}^0_l \subset \mathbb{N}^0_l$ be the set of nodes that sit strictly inside of $\mathbb{N}^0_l$ (i.e., excluding the outermost layer). The nodes of $\mathbb{M}^0_l$ that sit inside of the physical domain Ω_l are $\mathbb{M}^+_l = \mathbb{M}^0_l \cap \Omega_l$, and the exterior nodes are $\mathbb{M}^-_l = \mathbb{M}^0_l \cap \Omega^c_l$ (the complement of Ω_l). Note that specifically, the nodes of $\mathbb{M}^+_1$ lie inside the boundaries of the square and outside the circle (Fig. 9a), while the nodes of $\mathbb{M}^+_2$ fall inside the circle itself. Let $\mathbb{N}^+_l$ ($\mathbb{N}^-_l$) consist of the nodes obtained when applying $\mathcal{L}^{(h)}_l$ to the nodes of $\mathbb{M}^+_l$ ($\mathbb{M}^-_l$). The sets $\mathbb{N}^+_l$ and $\mathbb{N}^-_l$ are depicted in Fig. 9b, c. Then $\mathbb{N}^+_l$ and $\mathbb{N}^-_l$ will have a set of overlapping nodes near the boundary of Ω_l. This set of nodes is $\gamma_l = \mathbb{N}^+_l \cap \mathbb{N}^-_l$, and is referred to as the discrete boundary.

In order to simplify notation, the index l will also be dropped. Many of the definitions and results in Sect. 3.2 are defined identically for both parts of the subdomain, so grid sets and operators should be interpreted as consistent within their particular subdomain.

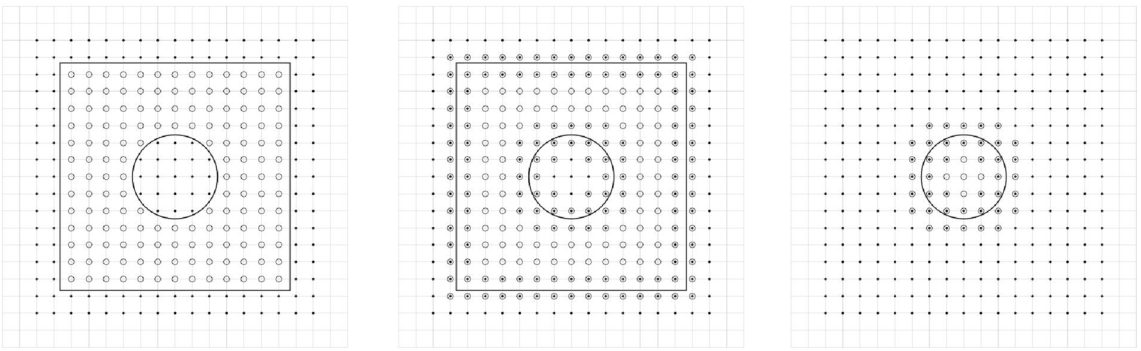

(a) $\circ - \mathbb{M}^+_1$ $\cdot - \mathbb{M}^-_1$ **(b)** $\circ - \mathbb{N}^+_1$ $\cdot - \mathbb{N}^-_1$ $\odot - \gamma_1$ **(c)** $\circ - \mathbb{N}^+_2$ $\cdot - \mathbb{N}^-_2$ $\odot - \gamma_2$

Fig. 9 Depictions of several grids sets. For each, $\mathbb{N}^0$ is the underlying mesh of grid nodes

3.2.1 Difference potentials and projections

Consider a grid function ξ_γ specified on the discrete boundary γ. We then define the *difference potential with density* ξ_γ as

$$P_{\mathbb{N}^+}\xi_\gamma \overset{\text{def}}{=} w - \mathcal{G}^{(h)}\left(\mathcal{L}^{(h)}w|_{\mathbb{M}^+}\right), \quad \text{where} \quad w = \begin{cases} \xi_\gamma & \text{on } \gamma \\ 0 & \text{on } \mathbb{N}^0\backslash\gamma \end{cases} \tag{11}$$

The difference potential (11) truncated to the grid boundary γ defines the *discrete boundary projection operator* P_γ

$$P_\gamma\xi_\gamma \overset{\text{def}}{=} \left(P_{\mathbb{N}^+}\xi_\gamma\right)\big|_\gamma \equiv Tr^{(h)}(P_{\mathbb{N}^+}\xi_\gamma) \tag{12}$$

where the operator $Tr^{(h)}$ refers to trace (truncation) of the grid set to its associated boundary γ. The projection P_γ given by (12) has the following key property:

Theorem 1 (Ryaben'kii) *A grid function ξ_γ satisfies the difference boundary equation with projection* (*BEP*)

$$P_\gamma\xi_\gamma + Tr^{(h)}\mathcal{G}^{(h)}g = \xi_\gamma \tag{13}$$

if and only if there is a solution u on $\mathbb{N}^+$ to the finite difference equation $\mathcal{L}^{(h)}u = g$ such that ξ_γ is the trace of u on the grid boundary γ, i.e., $\xi_\gamma = Tr^{(h)}u$.

The proof of Theorem 1 (as well as that of the projection property, $P_\gamma^2 = P_\gamma$) can be found in [13, Part II, Chapter 2]. If the BEP (13) holds for ξ_γ on γ, then the solution u can be reconstructed on $\mathbb{N}^+$ by means of the discrete generalized Green's formula:

$$u = P_{\mathbb{N}^+}\xi_\gamma + \mathcal{G}^{(h)}g \tag{14}$$

3.2.2 Equation-based extension

In order to guarantee the grid function ξ_γ in (14) accurately represents the continuous boundary data of the solution, we use an *extension operator*. For a given boundary Γ (either $\Gamma = \partial\Omega_1$ or $\Gamma = \partial\Omega_2$), consider a pair of functions (ξ_0, ξ_1) defined along Γ. One can consider these two functions as the Dirichlet and Neumann data, respectively, of some underlying function $v = v(x, y)$ on Ω^0:

$$(\xi_0, \xi_1) = \left(v, \frac{\partial v}{\partial \mathbf{n}}\right)\Big|_\Gamma$$

Near Γ, the function v can be expanded into a truncated Taylor series, where ρ represents the (unsigned) distance from the point of evaluation to the nearest point on Γ:

$$v(x,y) \overset{\text{def}}{=} v\,|_\Gamma + \rho\frac{\partial v}{\partial \mathbf{n}}\Big|_\Gamma + \frac{\rho^2}{2}\frac{\partial^2 v}{\partial \mathbf{n}^2}\Big|_\Gamma + \frac{\rho^3}{6}\frac{\partial^3 v}{\partial \mathbf{n}^3}\Big|_\Gamma + \frac{\rho^4}{24}\frac{\partial^4 v}{\partial \mathbf{n}^4}\Big|_\Gamma \tag{15}$$

Discussion and results pertaining to the number of terms included in this expansion can be found in [12, 31, 35], and trace back to formal results by Reznik [30, 36].

When the functions ξ_0 and ξ_1 are given, the first two terms of (15) can be computed directly. For the higher-order derivative terms, formulas can be produced by using equation-based differentiation applied to the Helmholtz equation (1a), where we assume v is a solution and v and $\frac{\partial v}{\partial \mathbf{n}}$ are known analytically on Γ.

For example, when Γ is the right side of a square (where $x = X$ is constant), the outward normal derivative coincides with the positive x–derivative. By substituting $v = \xi_0$ and $\frac{\partial v}{\partial \mathbf{n}} = \xi_1$, we can obtain the following sequence of formulas (see [12] for details on this derivation):

$$\begin{aligned}
v(X,y) &= \xi_0(y) \\
\frac{\partial v}{\partial x}(X,y) &= \xi_1(y) \\
\frac{\partial^2 v}{\partial x^2}(X,y) &= f(X,y) - \xi_0''(y) - k^2\xi_0(y) \\
\frac{\partial^3 v}{\partial x^3}(X,y) &= \frac{\partial f}{\partial x}(X,y) \\
&\quad - \xi_1''(y) - k^2\xi_1(y) \\
\frac{\partial^4 v}{\partial x^4}(X,y) &= \frac{\partial^2 f}{\partial x^2}(X,y) \\
&\quad - \frac{\partial^2 f}{\partial y^2}(X,y) - k^2 f(X,y) \\
&\quad + \xi_0^{(4)}(y) + 2k^2\xi_0^{(2)}(y) + k^4\xi_0(y)
\end{aligned} \tag{16}$$

Such formulas can also be obtained for the other sides of a square by substituting the boundary coordinates and appropriately identifying the outward normal derivatives, for example on the left side the outward normal derivative coincides with the *negative* x–derivative.

Additionally, when considering the rod subdomain there is a circular piece of the boundary that requires its own extension. Using the same general expansion (15), we recast the Helmholtz equation (1a) in polar coordinates (r, θ):

$$\frac{1}{r}\frac{\partial u}{\partial r} + \frac{\partial^2 u}{\partial r^2} + \frac{1}{r^2}\frac{\partial^2 u}{\partial \theta^2} = f$$

Consider the case of the interior of the rod so that the outward normal derivative coincides with the positive r–derivative (at $r = R$ a constant). The functions ξ_0 and ξ_1 then depend on θ and the following equations are obtained (as in [35]):

$$
\begin{aligned}
v(R,\theta) &= \xi_0(\theta)\\
\frac{\partial v}{\partial r}(R,\theta) &= \xi_1(\theta)\\
\frac{\partial^2 v}{\partial r^2}(R,\theta) &= f(R,\theta) - \frac{1}{R}\xi_1(\theta) - \frac{1}{R^2}\xi_0''(\theta) - k^2\xi_0(\theta)\\
\frac{\partial^3 v}{\partial r^3}(R,\theta) &= \frac{\partial f}{\partial r}(R,\theta)\\
&\quad - \frac{1}{R}\frac{\partial^2 v}{\partial r^2}(R,\theta) + \frac{1}{R^2}\xi_1(\theta)\\
&\quad + \frac{2}{R^3}\xi_0''(\theta) - \frac{1}{R^2}\xi_1''(\theta) - k^2\xi_1 \qquad (17)\\
\frac{\partial^4 v}{\partial r^4}(R,\theta) &= \frac{\partial^2 f}{\partial r^2} - \frac{2}{R^3}\xi_1(\theta)\\
&\quad + \left(\frac{2}{R^2} - k^2\right)\frac{\partial^2 v}{\partial r^2}(R,\theta) - \frac{1}{R}\frac{\partial^3 v}{\partial r^3}(R,\theta)\\
&\quad + \left(\frac{k^2}{R^2} - \frac{6}{R^4}\right)\xi_0''(\theta) + \frac{5}{R^3}\xi_1''(\theta)\\
&\quad - \frac{1}{R^2}\left(\frac{\partial^2 f}{\partial\theta^2}(R,\theta) - \frac{1}{R^2}\xi_0^{(4)}(\theta)\right)
\end{aligned}
$$

where $\xi_0^{(4)}(\theta)$ represents the fourth derivative of $\xi_0(\theta)$ with respect to θ. Note that when considering the circle from outside the rod, the outward normal derivative will instead coincide with the *negative* r–derivative.

The expressions from either (16), (17), or their appropriate analogs can be substituted into (15) to construct $v = v(x, y)$ from any pair of functions (ξ_0, ξ_1) defined on Γ. Sampling this function v only at nodes of the grid boundary γ defines the extension operator $\mathbf{Ex}$ that gives the grid function ξ_γ:

$$\xi_\gamma = \mathbf{Ex}(\xi_0, \xi_1) = v|_\gamma$$

As seen in (16) and (17) the extension operator depends on the source term f. The constribution from the source term makes $\mathbf{Ex}$ an affine operator:

$$\mathbf{Ex}\xi_\Gamma = \mathbf{Ex}^{(H)}(\xi_0, \xi_1) + \mathbf{Ex}^{(I)}f$$

$\mathbf{Ex}^{(H)}$ (homogeneous) operator acts only on the input functions (ξ_0, ξ_1), while the $\mathbf{Ex}^{(I)}$ (inhomogneous) operator is dependent on the source function f from the original problem (1a).

We emphasize that although (1a) was used to construct the expressions of (16) and (17), $\xi_\Gamma = (\xi_0, \xi_1)$ does not need to represent the Cauchy data of a solution u to (1a) in order to apply the operator $\mathbf{Ex}$. However, if ξ_Γ does correspond to the trace of a solution u, i.e., $\xi_\Gamma = \left(u, \frac{\partial u}{\partial \mathbf{n}}\right)\Big|_\Gamma$, then $\xi_\gamma = \mathbf{Ex}\xi_\Gamma$ approximates u with fifth-order accuracy near Γ with respect to the grid size, specifically at the nodes of ξ_γ.

3.2.3 Spectral representation at the boundary

Following the example of our previous work [12] we define a series representation of the boundary data, with the additional consideration of the central circle. Consider the breakdown of the boundary Γ in Fig. 10. For each Γ_i, choose a set of M_i basis functions $\{\psi_j\}_{j=1}^{M_i}$ such that each ψ_j is supported only on its corresponding Γ_i.

Generally speaking, each set $\{\psi_j\}_{j=1}^{M_i}$ can be chosen independently. For this particular setup, we use Chebyshev polynomials along the square edges $\Gamma_1, ..., \Gamma_4$ and Fourier basis functions around the central circle boundary Γ_5. To further simplify equations later on, we take each Chebyshev basis to have the same dimension, M_c, and pick the Fourier basis along Γ_5 such that $M_5 = |\{\psi_j\}_{-M_r}^{M_r}| = 2M_r + 1$. Given these specifications, we can define a larger set of basis functions $\{\Psi_j\}$ such that

$$\{\Psi_j\}_{j=1}^{M} = \underbrace{\{\psi_j\}_{j=1}^{M_c} \cup \{\psi_j\}_{j=1}^{M_c} \cup \{\psi_j\}_{j=1}^{M_c} \cup \{\psi_j\}_{j=1}^{M_c}}_{\Gamma_1,\ldots,\Gamma_4} \cup \underbrace{\{\psi_j\}_{-M_r}^{M_r}}_{\Gamma_5} \qquad (18)$$

where $M = 4M_c + 2M_r + 1$. Using the basis functions $\{\Psi_j\}$ defined in (18), consider the following pairs:

$$\mathbf{\Psi}_j^{(0)} = (\Psi_j, 0), \quad \mathbf{\Psi}_j^{(1)} = (0, \Psi_j), \quad j = 1, ..., M \qquad (19)$$

For boundary data of the form $\xi_\Gamma = (\xi_0, \xi_1)$, the pairs defined in (19) allow the components ξ_0 and ξ_1 to be expanded individually. Note that the set of functions used to define $\mathbf{\Psi}_j^{(0)}$ could be different from those used to define $\mathbf{\Psi}_j^{(1)}$, but for simplicity we use the same sets. Assume the boundary data of the solution we seek is given in the form $\xi_\Gamma = \left(u, \frac{\partial u}{\partial \mathbf{n}}\right)\Big|_\Gamma$, then that data can be expressed as the following series representation

$$\xi_\Gamma = \sum_{j=1}^{M} \mathbf{c}_j^{(0)}\mathbf{\Psi}_j^{(0)} + \sum_{j=1}^{M} \mathbf{c}_j^{(1)}\mathbf{\Psi}_j^{(1)} \qquad (20)$$

where $\mathbf{c}_j^{(0)}$ and $\mathbf{c}_j^{(1)}$ are the unknown expansion coefficients of the Dirichlet and Neumann data, respectively. For smooth boundary data, the Chebyshev and Fourier expansions converge rapidly, making the truncated terms of the expansion negligible with respect to the accuracy attainable on the grid for relatively small values of M_c and M_r.

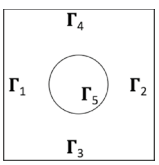

Fig. 10 Breakdown of the portions of Γ in the rod subdomain

The series (20) is defined in relation to the subdomain $\Omega_{j,1}$ (as in Fig. 10). One could similarly define a series representation of the solution at the boundary of $\Omega_{j,2}$ as well, but instead we remark that along $\overline{\Omega}_{j,1} \cap \overline{\Omega}_{j,2}$ (i.e., the circle) we know that $u_{j,1} = u_{j,2}$ and $\frac{\partial u_{j,1}}{\partial \mathbf{n}}_{j,1} = -\frac{\partial u_{j,2}}{\partial \mathbf{n}}_{j,2}$, allowing the portion (18) corresponding to Γ_5 to be reused when considering $\Omega_{j,2}$. This notion is utilized and further explained in Sect. 3.3.2.

3.3 Linear system

Consider a rod subdomain $\Omega_j = \Omega_{j,1} \cup \Omega_{j,2}$ with $\Gamma = \partial\Omega_{j,1}$. Let u be a solution to () over Ω_j and let $\xi_\Gamma = \left(u, \frac{\partial u}{\partial \mathbf{n}}\right)\Big|_\Gamma$ be the trace of the Dirichlet and Neumann data of the solution at the boundary. Let ξ_γ be given by applying $\mathbf{Ex}$ operator to the series representation (20) of the solution at the boundary of $\Omega_{j,1}$:

$$\begin{aligned}\xi_\gamma := \mathbf{Ex}\,\xi_\Gamma &= \mathbf{Ex}^{(H)}\left(\sum_{j=1}^{M} \mathbf{c}_j^{(0)}\boldsymbol{\Psi}_j^{(0)} + \sum_{j=1}^{M} \mathbf{c}_j^{(1)}\boldsymbol{\Psi}_j^{(1)}\right) + \mathbf{Ex}^{(I)} f \\ &= \sum_{j=1}^{M} \mathbf{c}_j^{(0)}\mathbf{Ex}^{(H)}\,\boldsymbol{\Psi}_j^{(0)} + \sum_{j=1}^{M} \mathbf{c}_j^{(1)}\mathbf{Ex}^{(H)}\,\boldsymbol{\Psi}_j^{(1)} + \mathbf{Ex}^{(I)} f\end{aligned} \tag{21}$$

The right-hand side of (21) can then be substituted into the discrete BEP (13) for $\Omega_{j,1}$. After rearranging terms, the following system is obtained:

$$\begin{aligned}&\sum_{j=1}^{M} \mathbf{c}_j^{(0)}(P_\gamma - I_\gamma)\mathbf{Ex}^{(H)}\,\boldsymbol{\Psi}_j^{(0)} + \sum_{j=1}^{M} \mathbf{c}_j^{(1)}(P_\gamma - I_\gamma)\mathbf{Ex}^{(H)}\,\boldsymbol{\Psi}_j^{(1)} \\ &\quad = \underbrace{(I_\gamma - P_\gamma)\mathbf{Ex}^{(I)} f - Tr^{(h)}\mathcal{G}^{(h)}\mathcal{B}^{(h)} f}_{F}\end{aligned} \tag{22}$$

where the coefficients $\mathbf{c}_j^{(0)}$ and $\mathbf{c}_j^{(1)}$ are the unknowns and I_γ represents the identity operator on γ. Letting F represent the right-hand side of (22) allows this equation to be expressed more compactly as

$$Q\mathbf{c} = F \tag{23}$$

where Q and c have the following forms:

$$\begin{aligned}Q = \Big[&\underbrace{(P_\gamma - I_\gamma)\mathbf{Ex}\,\boldsymbol{\Psi}_1^{(0)}, \ldots, (P_\gamma - I_\gamma)\mathbf{Ex}\,\boldsymbol{\Psi}_M^{(0)}}_{Q^{(0)}}, \\ &\underbrace{(P_\gamma - I_\gamma)\mathbf{Ex}\,\boldsymbol{\Psi}_1^{(1)}, \ldots, (P_\gamma - I_\gamma)\mathbf{Ex}\,\boldsymbol{\Psi}_M^{(1)}}_{Q^{(1)}}\Big] \\ \mathbf{c} = [&\underbrace{\mathbf{c}_1^{(0)}, \ldots, \mathbf{c}_M^{(0)}}_{c^{(0)\intercal}}, \underbrace{\mathbf{c}_1^{(1)}, \ldots, \mathbf{c}_M^{(1)}}_{c^{(1)\intercal}}]^\intercal\end{aligned} \tag{24}$$

where the dimensions of Q are $\gamma \times 2M$. In addition to (23), consider the contributions from the rod, $\Omega_{j,2}$. Let $\Gamma_r = \partial\Omega_{j,2}$ and repeat the steps above for the boundary data ξ_{Γ_r} to obtain a separate system corresponding to the scattering rod:

$$Q_r\mathbf{c}_r = F_r \tag{25}$$

In (25), $\mathbf{c}_r$ represents the coefficients of the expansion of the boundary data along the circle Γ_r and F_r is an analog to the right-hand side of (22) when the discrete boundary is γ_r instead of γ. The matrix $Q_r = \left[Q_r^{(0)}, Q_r^{(1)}\right]$ has a form similar to Q from (24), with dimensions $\gamma_r \times \left(4M_r + 2\right)$. The expansions of the Dirichlet and Neumann data along Γ_r each use $2M_r + 1$ Fourier basis functions since Γ_r contains only the circular boundary of the rod.

Note that the solutions of (23) and (25) are not unique because the BEPs (13) were derived only from the Helmholtz equation (1a). Additional equations are needed to supplement the system and make the solution $\mathbf{c}$ unique, although the exact nature of these conditions depends on the context. Section 3.3.1 explains how to derive such equations from local ABCs given on the exterior edges of $\partial\Omega_{j,1}$. When an edge of $\partial\Omega_{j,1}$ creates an interface with another subdomain, conditions can be derived as in [12]. In Sect. 3.3.2, we explain how to use the interface conditions between $\Omega_{j,1}$ and the rod $\Omega_{j,2}$.

3.3.1 Resolving the local ABCs

Consider the second-order Engquist-Majda ABC (3):

$$ik\frac{\partial u}{\partial \mathbf{n}} - k^2 u - \frac{1}{2}\frac{\partial^2 u}{\partial \tau^2} = 0 \tag{26}$$

Our goal is to substitute the series representations of the Dirichlet and Neumann data into (26). Without loss of generality, consider the series representation of the boundary data along one side of the exterior of the square subdomain and pass it into condition (26):

$$\begin{aligned}ik\left(\sum_{l=1}^{M_c} \mathbf{c}_l^{(1)}\psi_l\right) - k^2\left(\sum_{l=1}^{M_c} \mathbf{c}_l^{(0)}\psi_l\right) - \frac{1}{2}\frac{\partial^2}{\partial\tau^2}\left(\sum_{l=1}^{M_c} \mathbf{c}_l^{(0)}\psi_l\right) = 0 \\ \sum_{l=1}^{M_c}\left(ik\mathbf{c}_l^{(1)} - k^2\mathbf{c}_l^{(0)}\right)\psi_l - \frac{1}{2}\left(\sum_{l=1}^{M_c} \mathbf{c}_l^{(0)}\frac{\partial^2}{\partial\tau^2}\psi_l\right) = 0\end{aligned} \tag{27}$$

The formulation does not include a direct substitution for tangential derivatives (only the solution and its normal derivative). Instead, the second tangential derivative $\frac{\partial^2}{\partial\tau^2}$ is passed onto the basis functions and computed directly.

Along the edge of the square, tangential derivatives of the Chebyshev basis functions $\{\psi_l\}_1^{M_c}$ correspond to standard

derivatives with respect to the argument. Given the Chebyshev coefficients of a function (i.e., $\{\mathbf{c}_l^{(0)}\}$), the coefficients of the second derivative (i.e., $\{d_l\}$) can be computed with the following formula, adapted from [37]:

$$a_l d_l = 2 \cdot \sum_{j=1}^{\infty} j \cdot (l+j) \cdot (l+2j) \cdot \mathbf{c}_{l+2j}^{(0)}, \quad a_l = \begin{cases} 2, & l = 0 \\ 1, & l > 0 \end{cases}$$

The needed coefficients, $\{\mathbf{c}_l^{(0)}\}$ are unknown, so the formula is instead applied to each basis function individually to construct a matrix $A = [A_{i,j}]$ that represents the second derivative of the sum:

$$\begin{aligned} \frac{\partial^2}{\partial \tau^2} \sum_{l=1}^{M_c} \mathbf{c}_l^{(0)} \psi_l &= \sum_{l=1}^{M_c} \mathbf{c}_l^{(0)} \frac{\partial^2}{\partial \tau^2} \psi_l \\ &= \sum_{l=1}^{M_c} \mathbf{c}_l^{(0)} \left(\sum_{j=1}^{M_c} A_{l,j} \psi_j \right) \\ &= \sum_{l=1}^{M_c} \sum_{j=1}^{M_c} \mathbf{c}_l^{(0)} A_{l,j} \psi_j \\ &= \sum_{j=1}^{M_c} \psi_j \left(\sum_{l=1}^{M_c} \mathbf{c}_l^{(0)} A_{l,j} \right) \\ &= \sum_{j=1}^{M_c} \left(A_{*,j} \right)^{\intercal} \mathbf{c}^{(0)} \psi_j \end{aligned} \tag{28}$$

where row l of A corresponds to the coefficients of the second derivative of ψ_l, and $A_{*,j}$ indicates column j of A. Substituting (28) into (27) yields:

$$\sum_{l=1}^{M_c} \left(ik\mathbf{c}_l^{(1)} - k^2 \mathbf{c}_l^{(0)} \right) \psi_l - \frac{1}{2} \left(\sum_{l=1}^{M_c} \left(A_{*,l} \right)^{\intercal} \mathbf{c}^{(0)} \psi_l \right) = 0$$

$$\sum_{l=1}^{M_c} \left(ik\mathbf{c}_l^{(1)} - k^2 \mathbf{c}_l^{(0)} - \frac{1}{2} \left(A_{*,l} \right)^{\intercal} \mathbf{c}^{(0)} \right) \psi_l = 0$$

Orthogonality of the Chebyshev basis tells us that for each of $l = 1, ..., M_c$, we get a condition that relates the coefficients:

$$ik\mathbf{c}_l^{(1)} - k^2 \mathbf{c}_l^{(0)} - \frac{1}{2} \left(A_{*,l} \right)^{\intercal} \mathbf{c}^{(0)} = 0 \tag{29}$$

The conditions of (29) are coupled due to the third term, preventing them from being handled individually. Instead, consider them together as a matrix equation

$$\begin{aligned} ik\mathbf{c}^{(1)} - k^2 \mathbf{c}^{(0)} - \frac{1}{2} A^{\intercal} \mathbf{c}^{(0)} &= \vec{0} \\ -\left(k^2 I + \frac{1}{2} A^{\intercal} \right) \mathbf{c}^{(0)} + ik\mathbf{c}^{(1)} &= \vec{0} \end{aligned} \tag{30}$$

The relationship between $\mathbf{c}^{(0)}$ and $\mathbf{c}^{(1)}$ in (30) provides M_c supplemental conditions for system (23). This process is repeated for each side of the subdomain that contains an appropriate ABC.

It is well-known that matrices such as A in (30) can lead to poor conditioning, particularly when used in spectral solvers [38]. This problem more readily manifests itself in the presence of higher-order tangential derivatives (such as those that appear in higher-order Engquist-Majda ABCs). The numerical results we present in Sect. 4.1 suggest that such poor conditioning is avoided, for practical purposes, in the second-order condition we have chosen.

3.3.2 Resolving interface conditions along the rod

Let $\Gamma_5 \subset \partial\Omega_{j,1}$ be the circle from the boundary of $\Omega_{j,1}$ (as in Fig. 10) and $\Gamma_r = \partial\Omega_{j,2}$. Consider the following expansions of the boundary data along Γ_5 and Γ_r, respectively:

$$\begin{aligned} \xi_{\Gamma_5} &= \sum_{l=-M_r}^{M_r} \mathbf{c}_{5,l}^{(0)} \boldsymbol{\psi}_l^{(0)} + \sum_{l=-M_r}^{M_r} \mathbf{c}_{5,l}^{(1)} \boldsymbol{\psi}_l^{(1)} \\ \xi_{\Gamma_r} &= \sum_{l=-M_r}^{M_r} \mathbf{c}_{r,l}^{(0)} \boldsymbol{\psi}_l^{(0)} + \sum_{l=-M_r}^{M_r} \mathbf{c}_{r,l}^{(1)} \boldsymbol{\psi}_l^{(1)} \end{aligned} \tag{31}$$

Note that $\boldsymbol{\psi}_l^{(0)} = \left(\psi_l, 0 \right)$ and $\boldsymbol{\psi}_l^{(1)} = \left(0, \psi_l \right)$, as well as our choice that along these circles, the basis functions $\{\psi_l\}_{-M_r}^{M_r}$ are Fourier basis functions. Recall the interface conditions (5c) between two $\Omega_{j,1}$ and $\Omega_{j,2}$ and substitute the series representations of the Dirichlet and Neumann data from (31) into the interface conditions (5c):

$$\sum_{l=-M_r}^{M_r} \mathbf{c}_{5,l}^{(0)} \psi_l = \sum_{l=-M_r}^{M_r} \mathbf{c}_{r,l}^{(0)} \psi_l$$

$$\sum_{l=-M_r}^{M_r} \mathbf{c}_{5,l}^{(1)} \psi_l = -\sum_{l=-M_r}^{M_r} \mathbf{c}_{r,l}^{(1)} \psi_l$$

By moving terms to the same side, factoring out basis functions, and exploiting the orthogonality of the Fourier basis functions, we obtain conditions for each $l = -M_r, ..., M_r$ that couple together systems (23) and (25):

$$\mathbf{c}_{5,l}^{(0)} - \mathbf{c}_{r,l}^{(0)} = 0$$

$$\mathbf{c}_{5,l}^{(1)} + \mathbf{c}_{r,l}^{(1)} = 0$$

4 Numerical results

In this section, numerical results are presented that demonstrate the performance of our method. The first part, Sect. 4.1, focuses on smaller, simpler examples that explore the discretization error of the method as well as the reflection error

introduced by the absorbing boundary condition. Section 4.2 demonstrates more complex examples that are designed to more accurately represent a real PCRR. Demonstrative simulations are shown for linear waveguides (Sect. 4.2.1) as well as PCRR add/drop filters (Sect. 4.2.2).

For the results of this section, domains are constructed from collections of empty and rod subdomains (see Sect. 2.2), with interfaces between neighboring squares handled as discussed in [12]. The sides of each square have a length of 2 and the rods have a radius of 0.37 (this selection is explained in Sect. 4.2). Every subdomain is discretized independently by grids consisting of $(n+1)\times(n+1)$ nodes, with $n = 2^m$, in order to take full advantage of the efficiency of the Fourier transform used in the AP solver. Once the entire configuration of interest (such as a PCRR of Sect. 4.2) is assembled from elementary blocks—squares with or with no rods, one obtains a system of linear algebraic equations with respect to the unknown coefficients of expansions (20) along the boundaries of all subdomains. Those include interfaces between neighboring squares, rod interfaces, and outer boundaries where the ABCs are set (Sect. 3.3.1). This system is solved in the sense of least squares with the help of QR-factorization, see [12] for detail.

Throughout these results, two kinds of errors are used to discuss convergence. First, we consider errors in the traditional sense:

$$\|u^{(n)} - u\|_\infty \to 0 \quad \text{as } n \to \infty \tag{32}$$

In this case, $u^{(n)}$ refers to the solution computed using $n \times n$ grid nodes per subdomain and u is the true solution (when such a function can be derived). When a true solution cannot be derived, we instead assess the grid convergence by evaluating the norm of the difference between two succeeding approximate solutions obtained on a sequence of refined grids:

$$\|u^{(n)} - u^{(2n)}\|_\infty \to 0 \quad \text{as } n \to \infty \tag{33}$$

Proper grid convergence in the sense of (32) clearly implies (33). Additionally, if (32) is characterized by a certain convergence rate, then the rate characterizing (33) will be at least as fast.

4.1 Preliminary simulations

In order to evaluate the discretization error of the method and the reflection error introduced by the local ABC, an exact solution needs to be constructed for reference. For simplicity, the discretization and reflection errors are only computed directly in the rod subdomain for cases where the wavenumber is constant between the rod and the rest of the subdomain (i.e., $k_1 = k_2 = k$).

Consider the Green's function:

$$G(x,y) = \frac{i}{4}H_0^{(1)}(k\sqrt{x^2+y^2}) \tag{34}$$

where k is the wavenumber from (1a) and $H_0^{(1)}$ is the Hankel function. It is well-known that (34) satisfies the 2D Helmholtz equation with the point-source $f(x,y) = \delta(x,y)$ and the Sommerfeld radiation condition (2). However, the singularity at the origin of the Hankel function makes $G(x, y)$ ill-suited for numerical evaluation. Therefore, we instead consider a smoothed variation obtained by the following process:

1. Take the x–derivative of the fundamental solution ($G_x = \frac{\partial G}{\partial x}$). This will make the resulting test solution anisotropic, i.e., more generic than a centrally symmetric solution.
2. Construct a function, $\eta(r)$, which is equal to 0 at $r = 0$, equal to 1 when $r \geq R$, and is sufficiently smooth in $0 < r < R$. We use $R = \frac{1}{2}$ and require 5 vanishing derivatives at each endpoint, i.e., $\eta^{(d)}(0) = \eta^{(d)}(R) = 0$ for $d = 1, ..., 5$.
3. Multiply the smoothing function by the differentiated fundamental solution to obtain a new solution $u = G_x\eta$.

This function $u_{\text{rad}} = G_x\eta$ is a solution to the homogeneous Helmholtz equation (i.e., $f \equiv 0$) outside the radius of $R = \frac{1}{2}$. Inside that radius, the source function f can be derived by plugging u_{rad} into the Helmholtz equation and taking its derivatives analytically:

$$f = \frac{\partial^2}{\partial x^2}(G_x\eta) + \frac{\partial^2}{\partial y^2}(G_x\eta) + k^2 G_x\eta \tag{35}$$

For this paper, the derivatives in (35) were computed with the `diff` command from the symbolic computation toolbox in MATLAB. The function u_{rad} and its corresponding source function f can be seen in Fig. 11, and u_{rad} is used throughout Sects. 4.1.1 and 4.1.2 as a reference solution. The simulations of Sects. 4.1.3 and 4.2 are driven by the same source term f from (35).

4.1.1 Discretization error

To evaluate the discretization error introduced by the method, we compare the computed solution to the (exact) derived solution, $u_{\text{rad}} = G_x\eta$. This is done on a domain composed of an empty subdomain and a rod subdomain (see Fig. 12), where the empty subdomain is centered about the origin. The Dirichlet boundary conditions and source function (35) are computed directly from the exact solution u_{rad}. Table 1 demonstrates that the method achieves the design fourth-order convergence rate of the underlying finite difference method for a variety of wavenumbers.

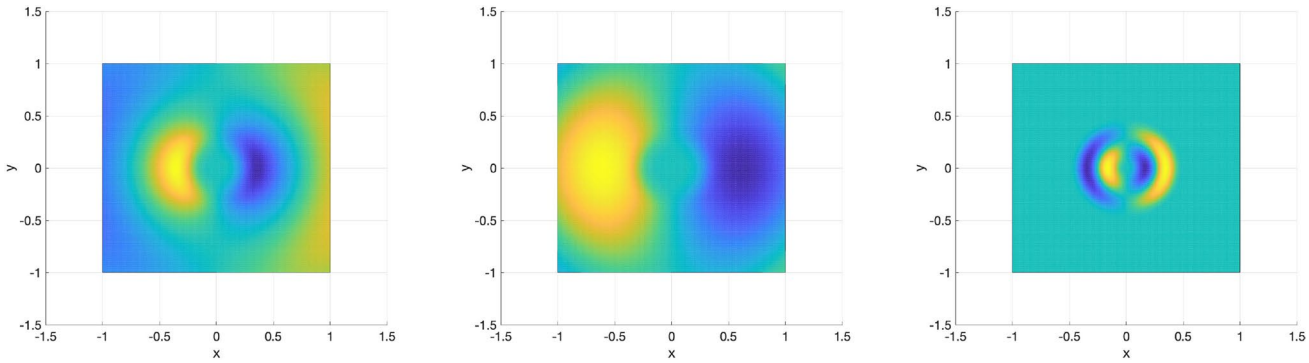

Fig. 11 Real part (left) and imaginary part (center) of the function u_{rad}, and the real part of the corresponding derived source function f (right), all plotted for the wavenumber $k = 3$

Fig. 12 Depiction of the domain used in Table 1

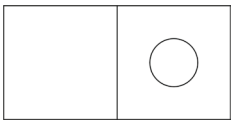

4.1.2 Reflection error

Similar to the discretization error, evaluation of the reflection error requires an exact solution for comparison. The function u_{rad} serves as the exact solution here as it did in Sect. 4.1.1, and the source term is provided by (35). At the outer boundary, the second-order Engquist-Majda absorbing boundary conditions (3) are applied to approximate the outgoing waves.

The reflection error is a property of the chosen boundary conditions and therefore independent of the grid discretization. An example of this can be seen in the grid convergence analysis of Table 2, where the method appears to be converging as expected (fourth-order) on coarser grids before the convergence levels off. This is the point at which the reflection error dominates the discretization error. Due to the choice of a high-order finite difference method, we generally expect this trade-off from discretization error to reflection error to happen at relatively coarse grids.

It is worth noting that the wavenumber chosen for Table 2 (and Fig. 13) is higher than the other choices throughout Sect. 4. For smaller wavenumbers, the reflection error dominates the discretization error even at the coarser grid levels (see Table 3). In fact, [18] provides the following approximation for the amplitude of reflected waves (denoted b) when using second-order Engquist-Majda absorbing boundary conditions:

$$b \approx a \left| \frac{\cos(\theta) - 1}{\cos(\theta) + 1} \right|^2 \tag{36}$$

where a is the amplitude of the incident wave and θ is the angle of incidence. The expression (36) is maximized when $\theta = \frac{\pi}{4}$, which occurs at the corners of the domain (visualized in Fig. 13. With this choice of θ, (36) reduces to

$$b \approx a \left| \frac{\cos(\frac{\pi}{4}) - 1}{\cos(\frac{\pi}{4}) + 1} \right|^2 \implies b \approx (0.0294)a \tag{37}$$

Roughly speaking, (37) tells us that the amplitude of the reflection error will be around 3% of the amplitude of the incident wave. To confirm this, the reflection error is evaluated across several domains for $k = 10$ and presented in Table 3.

Table 1 Discretization error $\|u^{(n)} - u\|_\infty$ and rate of convergence to the true solution $u = G_x\eta$ with $k = 5, 10$, and 15

n	$k = 5$		$k = 10$		$k = 15$	
	Error	Rate	Error	Rate	Error	Rate
64	1.22e−04	–	9.14e−04	–	4.86e−01	–
128	7.53e−06	4.02	5.69e−05	4.01	2.11e−03	7.84
256	4.25e−07	4.15	3.65e−06	3.96	1.28e−04	4.04
512	2.83e−08	3.91	2.27e−07	4.00	8.01e−06	4.00
1024	1.64e−09	4.11	1.43e−08	3.99	5.01e−07	4.00

Dirichlet boundary conditions and source function are derived from the solution

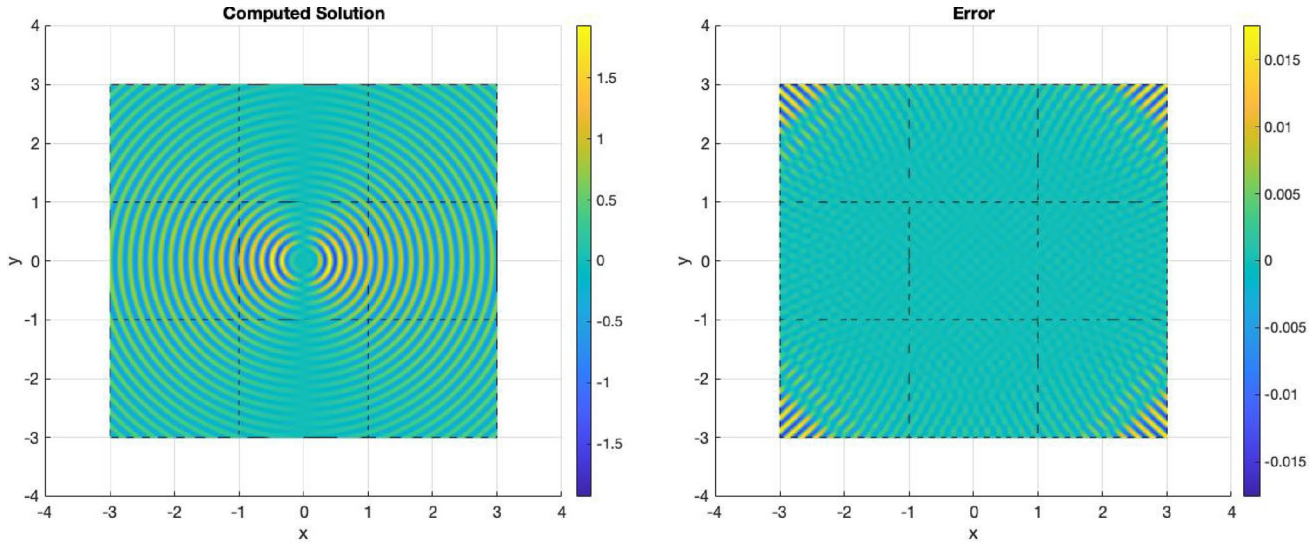

Fig. 13 Real parts of the computed solution approximating u_{rad} with $k = 40$ (left) and the error between the computed solution and u_{rad} (right), corresponding to Table 2. The domain is a 3×3 arrangement of empty subdomains, and each subdomain is discretized by a grid of 512×512 nodes

Table 2 Absolute reflection error and convergence rate for a 3×3 arrangement of empty subdomains with $k = 40$ (see Fig. 13) and second-order Engquist-Majda absorbing boundary conditions along the exterior edges

n	$\|u^{(n)} - u\|_\infty$	Rate
64	1.20e+02	–
128	4.38e+00	4.78
256	2.83e−01	3.95
512	1.76e−02	4.01
1024	1.76e−02	0.00
2048	1.76e−02	0.00

Note that the lack of convergence in Table 3 confirms that the reflection error is not dependent on the grid discretization. By comparing Table 3 with Table 1, it is clear that the discretization error for this solution is notably smaller than the reflection error. Further, note the improved performance as the size of the domain is increased. The reflection error is expected to decrease as the domain grows larger (and as the amplitude of the solution decreases), and this is confirmed in Table 3.

Tables 2 and 3 indicate that the reflection error prevents the computed solution from converging to the true solution, u_{rad}. The grid convergence, however, still takes place, albeit to a different solution that is subject to reflections from the artificial outer boundary due to boundary condition (26). This is corroborated by the data in Table 4 that shows convergence in the sense of (33).

4.1.3 Inclusion of scattering rods

By allowing a change in the wavenumber between the rod and the rest of the subdomain (i.e., $k_1 \neq k_2$), the refraction of a signal between two mediums can be simulated. We generally only consider the case of $k_1 < k_2$ which represents the case where the rod has a higher refractive index than its surrounding material. This formulation makes it difficult to compose an exact solution for reference to demonstrate grid convergence, so convergence is considered as

Table 3 Maximum absolute and relative reflection errors along the exterior edges of Ω

n	1×1		3×3		5×5	
	Absolute error	Relative error (%)	Absolute error	Relative error (%)	Absolute error	Relative error (%)
64	2.37e−02	3.80	1.08e−02	3.30	7.91e−03	2.89
128	2.59e−02	4.16	1.12e−02	3.42	7.81e−03	2.85
256	2.59e−02	4.16	1.12e−02	3.43	7.81e−03	2.86
512	2.65e−02	4.25	1.13e−02	3.45	7.85e−03	2.87

Computed for $k = 10$ for domains constructed from several arrangements of empty subdomains (1×1, 3×3, and 5×5)

Table 4 Convergence analysis with respect to the self-convergence metric from (33)

n	1×1		3×3		5×5	
	$\|u^{(n)} - u^{(2n)}\|_\infty$	Rate	$\|u^{(n)} - u^{(2n)}\|_\infty$	Rate	$\|u^{(n)} - u^{(2n)}\|_\infty$	Rate
64	4.09e−04	–	4.45e−04	–	6.17e−04	–
128	2.65e−05	3.95	2.84e−05	3.97	3.69e−05	4.06
256	1.82e−06	3.86	1.70e−06	4.06	2.26e−06	4.03
512	1.04e−07	4.13	1.09e−07	3.97	1.43e−07	3.98

Domains are composed of varying arrangements of empty subdomains (1×1, 3×3, and 5×5), and the wavenumber is $k = 10$

Table 5 Convergence analysis with respect to the self-convergence metric from (33) for examples with scattering rods

n	$k_1 = 1$		$k_1 = 3$	
	$k_2 = 3$		$k_2 = 10$	
	$\|u^{(n)} - u^{(2n)}\|_\infty$	Rate	$\|u^{(n)} - u^{(2n)}\|_\infty$	Rate
64	2.82e−01	–	6.84e−01	–
128	3.33e−04	9.73	2.54e−03	8.07
256	1.44e−05	4.53	6.56e−06	8.60
512	1.29e−06	3.48	3.57e−07	4.20

The domain is depicted in Fig. 12, with wavenumber jumps indicated from k_1 outside the rod to k_2 inside the rod

in (33). The domain is taken as in Fig. 12 with the source function (35) centered about the empty subdomain and second-order Engquist-Majda absorbing boundary conditions along the exterior of the domain. The convergence rate in Table 5 is indicative of the design fourth-order convergence rate as discussed earlier and demonstrated in Tables 1 and 4.

4.2 PCRR simulations

In this section, we present and discuss two forms of simulations associated with PCRRs. First is an isolated bus waveguide with a varying number of rows of scattering rods on either side of the channel. Second is the classic add-drop filter which can redirect a signal toward different output channels depending on the frequency.

As discussed in Sect. 4.1.2, the reflection error is expected to outweigh the discretization error, even at relatively coarse grids. Therefore, results are only reported on a single grid (indicated for each simulation). Additionally, we use a consistent setup scheme for determining the source function for each simulation (see Fig. 14). The source function f (from (35)) is placed between rows of scattering rods, such that one empty subdomain separates the source's subdomain from the left edge of the domain.

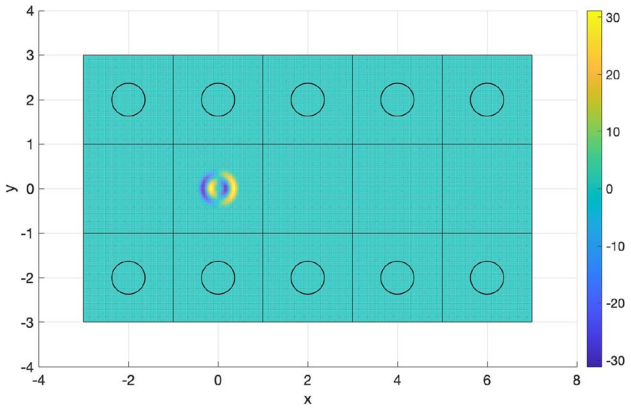

Fig. 14 An example of how the source function (35) is placed within a PCRR domain. The source is centered over one of the empty subdomains such that one empty subdomain sits between the source's support and the exterior boundary of the domain

This way, the source can emulate an input signal that is primarily traveling from the left to the right.

The parameters for the simulations are chosen to reflect those used in [1, Chapter 13]. The descriptions of the primary parameters are as follows:

- a = Lattice periodicity, or the shortest center-to-center distance between two rods. Consequently, a is also the length of each side of the subdomains.
- r = Radius of the scattering rods. The ratio of the radius of the rods to the lattice periodicity (i.e., r/a) is an important factor in determining valid frequencies for the PCRR.
- $n_{\text{air}}, n_{\text{rod}}$ = Refractive indices of the background (air) and scattering rods, respectively.

In [1, Chapter 13], the lattice periodicity is chosen as $a = 540$nm and the radius of the rods is $r = 100$nm, resulting in a ratio of $r/a \approx 0.185$. The refractive indices are selected to represent air ($n_{\text{air}} = 1.00$) and silicon ($n_{\text{rod}} = 3.48$). These parameters correspond to bus waveguides that support the near infrared wavelengths between approximately $\lambda = 1270$nm and $\lambda = 1780$nm.

For the simulations in this paper, the parameters have been nondimensionalized. The lattice periodicity (and side length of subdomains) is 2. In order to maintain the ratio of the rod radius to lattice periodicity, we take $r = 0.37 = 2 \times 0.185$ (hence the choice for the rod radius in the results of Sect. 4.1). The refractive indices provide a ratio for the wavenumbers we select, namely $k_2 = 3.48 \times k_1$. The background wavenumber k_1 can then be derived by equating the ratio of the lattice periodicity to the desired wavelength from each example, i.e.,

$$\begin{aligned} \text{(Physical)} \quad \frac{a}{\lambda} &= \frac{k_1 a}{2\pi} \quad \text{(Nondimensionalized)} \\ \frac{540}{\lambda} &= \frac{2k_1}{2\pi} \\ \frac{540\pi}{\lambda} &= k_1 \end{aligned} \tag{38}$$

Therefore, a physical wavelength of 1550nm approximately corresponds to a wavenumber of $k_1 = 1.08$. As our discretization is fourth-order accurate, for this low value of the wavenumber the error due to the second-order Engquist-Majda boundary condition becomes dominant already on fairly coarse grids, see Sect. 4.1.2.

For most of the figures in this section, we have chosen to present the imaginary part of the solution. The real part of the source function has a high degree of variation at the origin, causing the real part of the resulting solution to have abnormally high variation near the source. However, the imaginary part changes much more gradually near the source, forming a much smoother and visually interpretable image while still demonstrating the same qualitative behaviors as its corresponding real part.

4.2.1 Bus waveguides

Recall that a ring resonator is constructed from two bus waveguides and a ring-shaped waveguide (Fig. 1). For the specific case of a PCRR (Fig. 1b) the bus waveguide can be isolated to make its own domain as in Fig. 15.

From [1], it is known that the number of rows of scattering rods on either side of the open channel largely affects how efficiently the channel propagates waves. Generally speaking, increasing the number of rows of rods will decrease the amount of leakage from the waveguide at the expense of more computation time to account for more rods. By computing the solution in domains with varying numbers of buffer rows of rods, we can observe how the solution changes to determine how many rows are needed to capture the qualitative behavior.

In order to analyze the impact of buffer rows of rods, we assemble a sequence of simulations that represent bus waveguides with varying numbers of buffer rows. Each problem uses the same source function from (35) placed in the waveguide as described in Fig. 14, along with second-order Engquist-Majda boundary conditions along the exterior edges of the relevant subdomains. The domain of interest is a 1×15 assembly of empty subdomains with the corresponding number of buffer rows of rod subdomains attached to both the top and bottom. The resulting computed solutions are collectively presented on the left side of Fig. 16. Note that the plots in Fig. 16 only represent the empty subdomains down the center of the domain.

The right side of Fig. 16 shows how the solution changes after each addition of a new buffer row of rod subdomains. The error is calculated as the absolute difference between two solutions within the empty subdomains, where the solution most clearly depicts a traveling wave. Notice that the signal is noticeably fuzzy in the first solution (top-left of Fig. 16), but becomes sharper when a second row of buffer rods is included. This difference is visualized in the first image of the right column, where it can clearly be seen that the difference between the two solutions grows toward the end of the domain. Although there is little visual difference between the cases of 2 and 3 buffers in the left column, the second error plot still shows a discernible change at the right end of the channel. Finally, the change when moving from 3 to 4 buffer rows is even less than the previous case, and visually negligible when compared to the previous cases.

Ideally, the number of buffer rows would be taken to infinity (or at least arbitrarily high) to provide the best

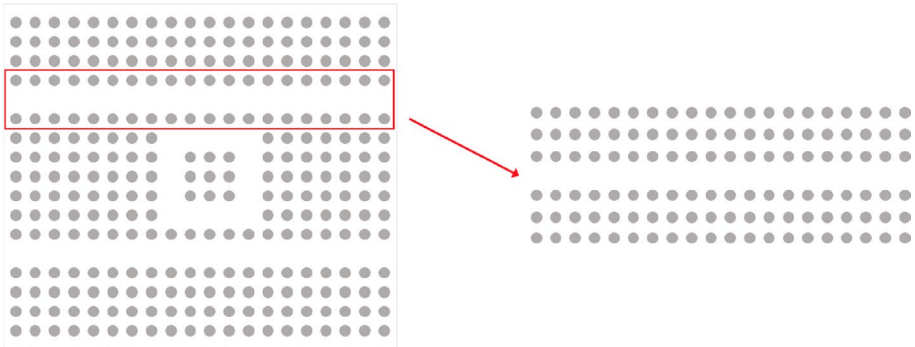

Fig. 15 One of the bus waveguides can be isolated and considered as its own domain

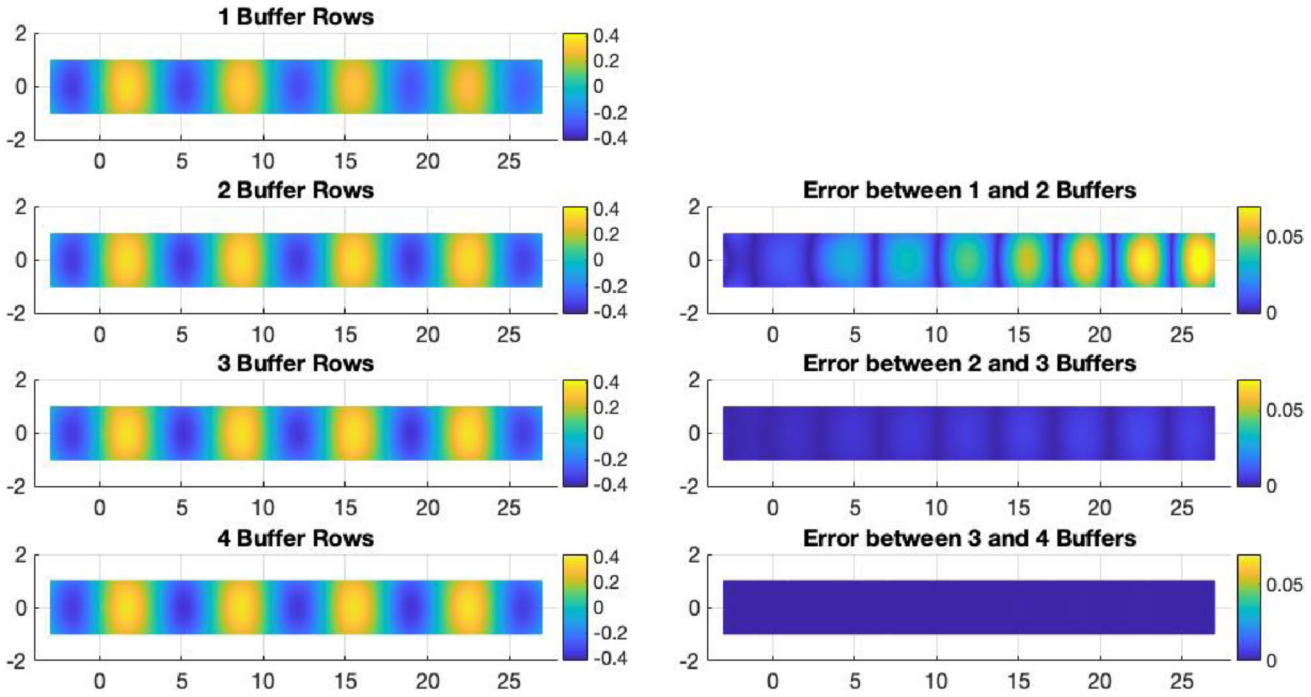

Fig. 16 (Left) Imaginary part of the solution for varying numbers of buffer rows of rods and (right) the absolute difference between a given solution and the preceding case. Plotted for $k = 1.229$ on a 129×129 grid for each subdomain

approximation, but this is obviously impractical. Referring to the case of 2 buffers, $\|u\|_\infty \approx 0.3256$ and the maximum error between the cases of 2 and 3 buffers is approximately 0.0067. Adding an extra row of buffers only improves the accuracy by 2%. Given that the reflection error from the ABCs is around 3%, 2 buffer layers are chosen for the larger simulations of the next section.

4.2.2 PCRR add-drop filter

The final set of simulations concern the functionality of a 2D PCRR add-drop filter. The only new feature introduced for this structure is the ring resonator itself. The resonator is formed in a similar fashion as the bus waveguides from Sect. 4.2.1, with the difference that the channel formed by removing rods is now a square (note Figs. 1b, 2, and 15). Note that the shape of the ring will depend on the symmetry of the lattice of rods; alternative arrangements (such as a hexagonal resonator) can be found in [1].

Following the square lattice example from [1], a PCRR is constructed around a resonator with a 3×3 set of rods at its center (as in Fig. 15). Bus waveguides are appended to the top and bottom of the resonator with one set of rods separating the bus waveguides from the resonator. One extra row of rods is included on the top and bottom of the domain to prevent leakage (following the example set by Sect. 4.2.1) forming a 13×15 lattice of subdomains as in Fig. 17. The system is driven by the source function f from (35), placed as

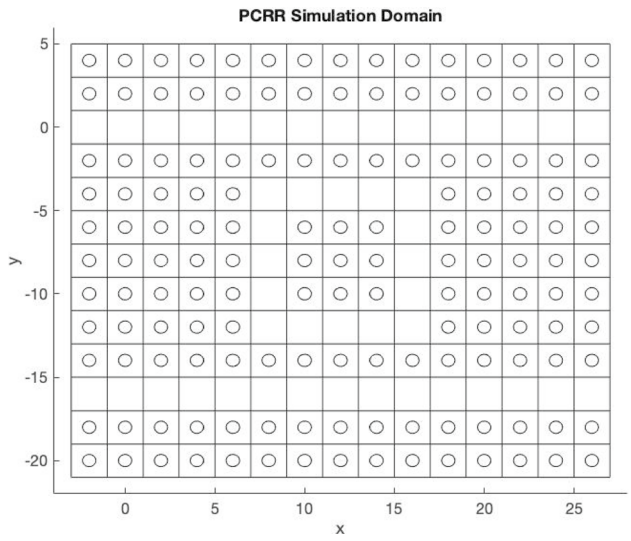

Fig. 17 The domain used for the PCRR simulations of Sect. 4.2.2. Solid lines denote interfaces between subdomains, and the source function is centered about the origin

in Fig. 14, which simulates an input signal from the top-left port with a given frequency. The frequency is determined by the wavenumber k in the corresponding Helmholtz equation, and the relationship of this k to a physical wavelength is given in (38).

The main simulations of focus are presented in Figs. 18 and 19. They represent two wavenumbers with qualitatively

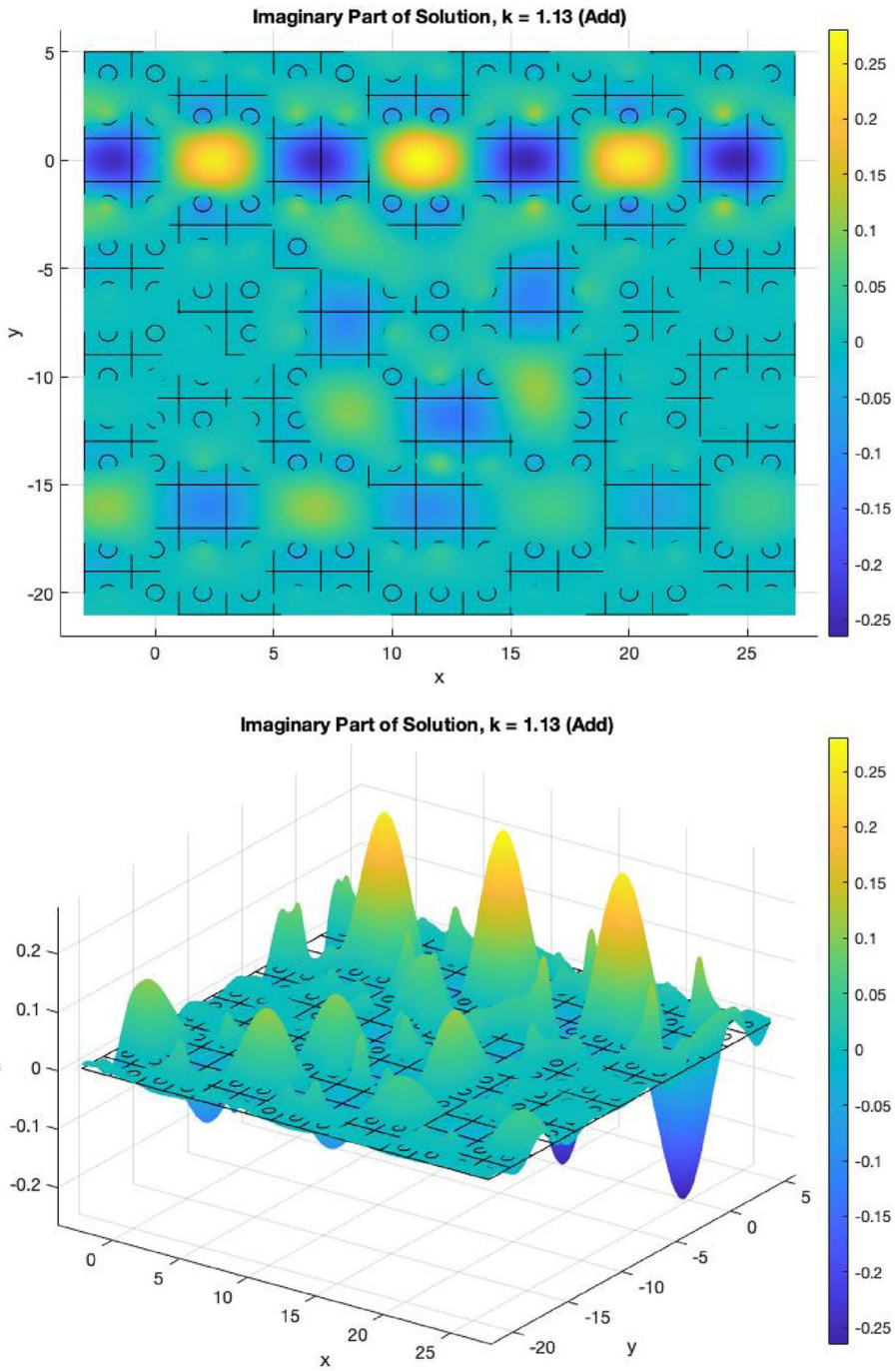

Fig. 18 Example of a PCRR operating at an add-frequency corresponding to the wavenumber $k = 1.13$. Each subdomain is discretized by a grid of 129×129 nodes

different behaviors in the PCRR. The first simulation, Fig. 18, represents a signal that is designed to pass through the device without being filtered. Some energy does spread throughout the domain, particularly through the channels, but this kind of leakage is to be expected given the use of discrete rods in place of continuous walls. The important piece, qualitatively speaking, is that the strength of the signal in the bottom bus waveguide is distinctly lower than in the top bus waveguide. For the second simulation, Fig. 19 represents a signal that the PCRR is designed to filter through the ring resonator. It is demonstrating the expected behavior, which is for the strength of the signal to be greater at the bottom-left port than either port on the right side of the domain.

Figures 20 and 21 provide examples of some of the alternative behaviors that the PCRR can express as the wavenumber/wavelength go further outside of the intended window of use for the parameters. In Fig. 20, the signal

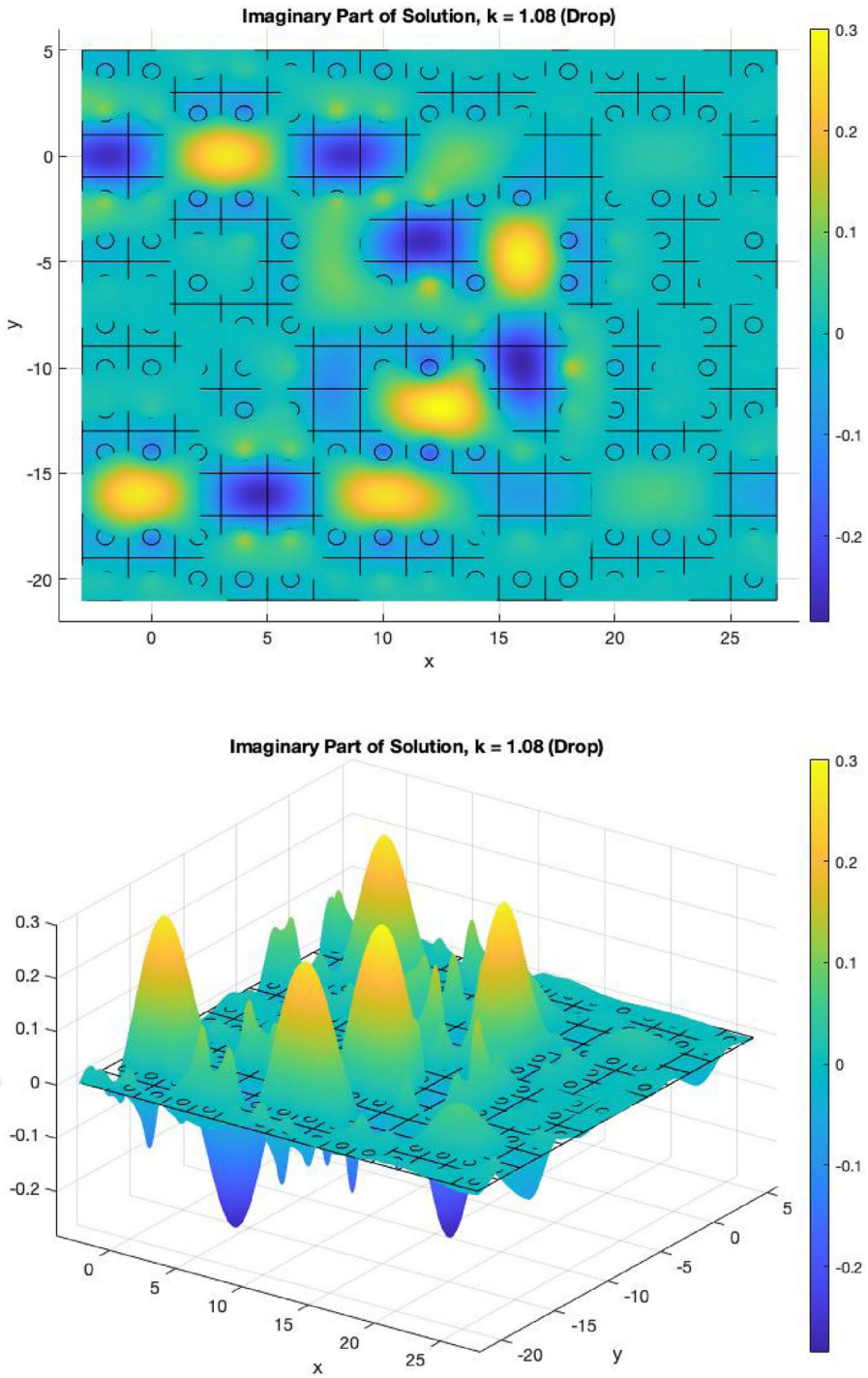

Fig. 19 Example of a PCRR operating at a drop-frequency corresponding to the wavenumber $k = 1.08$. Each subdomain is discretized by a grid of 129×129 nodes

drops from the top bus into the resonator, but not into the bottom bus. In Fig. 21, the signal is approximately as strong at the right end of the top bus as it is at the left end, but it enters the resonator just as in Fig. 20. These two examples demonstrate apparent deficiencies, which we believe to be attributed to the model as opposed to the method. A known problem for such PCRRs stems from the the fact that a square duct is used in place of a circle in the true ring resonator case, causing certain degenerative behaviors [1, Chapter 13]. The known way to combat this is by introducing four additional scattering rods in the corners of the resonator such that they are equidistant

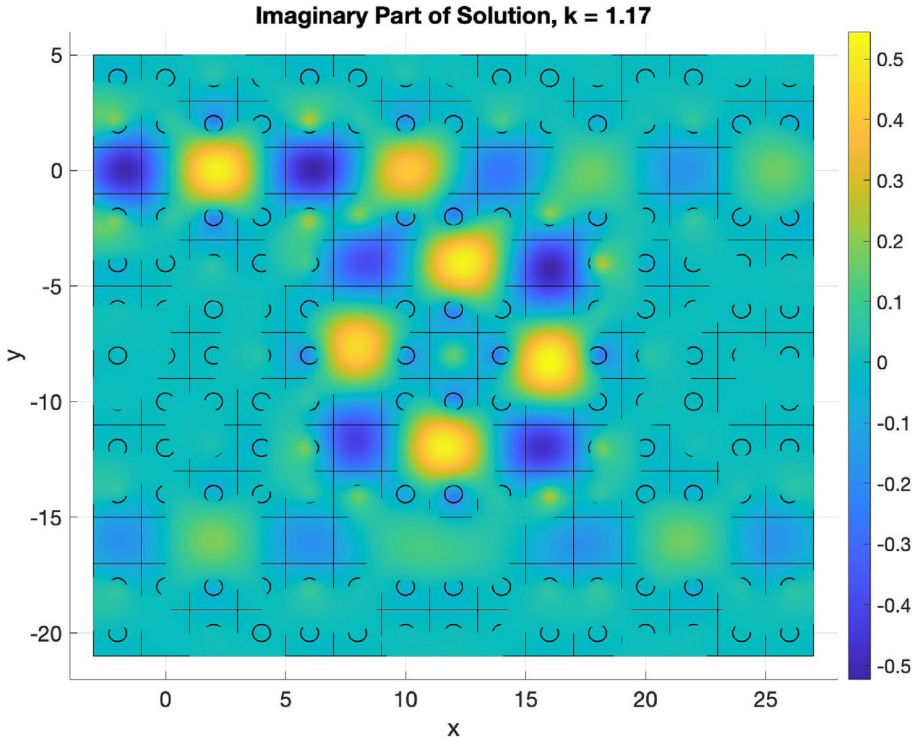

Fig. 20 Example of a PCRR operating at a resonant frequency corresponding to the wavenumber $k = 1.17$

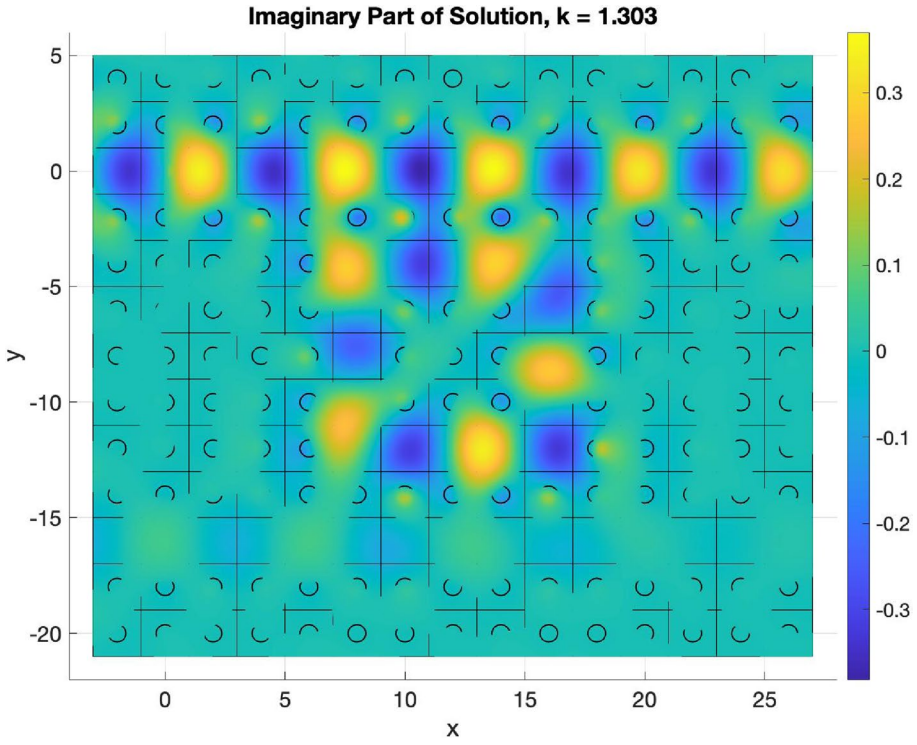

Fig. 21 Example of a PCRR operating at a resonant frequency corresponding to the wavenumber $k = 1.303$

from the three rods that currently form the corner. Unfortunately, these points are at the intersection of the building blocks, making this supplement incompatible with the framework in its current form. One potential solution is discussed in Sect. 5.

4.3 Time-harmonic versus time-dependent modeling

The simulations of waveguides and PCRRs in the current paper were conducted for the case of monochromatic waves

in the frequency domain, with the key governing equation being the Helmholtz equation (1a). Time-harmonic modeling of nano-scale devices is quite common in the literature, see, e.g., [39, 40] as well as [41] for a more general setting. For our simulations, we have assumed a silicon-on-insulator (SOI) structure of the photonic crystal operating in a near infrared regime. The rod material in a SOI photonic crystal is non-dispersive. However, time-harmonic approach applies to the case of dispersive materials as well, see, e.g., [40], where a metal-insulator-metal (MIM) structure is studied and the dielectric permittivity obeys the Drude model. A key advantage of time-harmonic simulations is that they are less costly compared to full time-domain modeling. At the same time, their key restriction is that, the excitation that drives the system shall be a genuine continuous wave (CW), i.e., a single-frequency signal. In the case of a broadband excitation (as opposed to CW), time-domain computations are warranted. Time-domain simulations of nanostructured devices have been reported, e.g., in [4, 7]. While the methodology of the current paper is designed for time-harmonic implementation, we note that, its core component, the method of difference potentials, applies to time-dependent problems as well and maintains high-order accuracy for non-conforming geometries, see, e.g., [42]. In future, it may be beneficial to look into how to extend the currently proposed domain decomposition algorithm based on the MDP to the case of time-dependent (broadband) simulations.

5 Conclusions and future work

The goal of this paper is to expand the framework introduced in [12] for solving domain decomposition problems with the MDP, and to demonstrate the method's ability to simulate 2D photonic crystal ring resonators in the monochromatic case. To this end, the "rod subdomain" was introduced and the implementation of local absorbing boundary conditions was described using the second-order Engquist-Majda conditions. Analysis of the discretization and reflection errors corroborated the design properties of the underlying finite difference method and ABCs. Those include high-order accuracy and non-deteriorating performance for non-conforming boundaries on Cartesian grids. Numerical simulations demonstrated that the method is able to properly capture the intended behavior of the PCRR. A key advantage of the proposed method is that, it allows to easily modify the configuration of interest. For example, rows of rods can be added or removed as in Sect. 4.2.1 and other modifications can be implemented by merely changing the arrangement of elementary blocks (subdomains with and with no rods) without having to recompute the Calderon's operators that pertain to those blocks.

To be able to capture sharper resonances and thus enable more accurate simulations of PCRRs by the proposed method, one direction for future work is to investigate how to incorporate scattering rods that do not fall in the center of the designed subdomains. For example, [1, Chapter 13] describes the addition of rods in the corners of the ring to improve the spectral selectivity. These particular locations fall on the corners of our existing subdomains and are not compatible with the method as presented here. One approach is to design larger "macro-blocks" that take the place of several subdomains at once, granting more freedom in how rods could be placed throughout that macro-block. Such an addition would increase the number of building blocks to be pre-computed, but could make the run-time computations more efficient.

Moving beyond the specific application of PCRRs, another future direction for the method as a whole is to change how the rod subdomain is handled. In its current form, the rod subdomain itself consists of two subdomains, with the transmission between the two subdomains being handled at the same time as the transmission between squares. If the operators for the two parts of the rod subdomain could be combined before run-time, then the dimension of the discrete BEP, and therefore the computation time of the QR-factorization (Sect. 4), could be reduced. The beneficial effect would continue to increase if multiple scattering objects were included within one subdomain. A subsequent extension of this idea could lead to a hierarchical domain decomposition algorithm. For example, one can build 2×2 macro-blocks out of 4 elementary subdomains by eliminating the interior interfaces ahead of time. Then, the resulting macro-blocks can be clustered further—in 2×2 structures on the next level, etc. This hierarchical construct will enable substantial savings in the overall cost of QR-factorization when solving for the coefficients of (20).

Acknowledgments Work supported by the US–Israel Binational Science Foundation (BSF) under Grant # 2020128.

Author contributions All authors contributed to the study conception and design. Numerical simulations were conducted by Evan North. The first draft of the manuscript was written by Evan North and all authors commented on previous versions of the manuscript. All authors read and approved the final manuscript

Data availability The datasets generated during and/or analyzed during the current study are available from the corresponding author on reasonable request.

Declarations

Conflict of interest The authors have no relevant financial or non-financial interests to disclose.

References

1. Chremmos, I., Uzunoglu, N.K., Schwelb, O. (eds.): Photonic Microresonator Research and Applications. Springer, New York (2010)
2. Fard, S.T., Grist, S.M., Donzella, V., Schmidt, S.A., Flueckiger, J., Wang, X., Shi, W., Millspaugh, A., Webb, M., Ratner, D.M., Cheung, K.C., Chrostowski, L.: Label-free silicon photonic biosensors for use in clinical diagnostics. In: Kubby, J., Reed, G.T. (eds.) Silicon Photonics VIII, vol. 8629, pp. 49–62. SPIE, Bellingham, WA (2013). https://doi.org/10.1117/12.2005832. International Society for Optics and Photonics
3. Amoosoltani, N., Mehrabi, K., Zarifkar, A., Farmani, A., Yasrebi, N.: Double-ring resonator plasmonic refractive index sensor utilizing dual-band unidirectional reflectionless propagation effect. Plasmonics **16**(4), 1277–1285 (2021). https://doi.org/10.1007/s11468-021-01395-9
4. Farmani, A.: Three-dimensional fdtd analysis of a nanostructured plasmonic sensor in the near-infrared range. J. Opt. Soc. Am. B **36**(2), 401 (2019). https://doi.org/10.1364/josab.36.000401
5. Farmani, A., Miri, M., Sheikhi, M.H.: Tunable resonant Goos-Hänchen and Imbert-Fedorov shifts in total reflection of terahertz beams from graphene plasmonic metasurfaces. J. Opt. Soc. Am. B **34**(6), 1097 (2017). https://doi.org/10.1364/josab.34.001097
6. Romero-Vivas, J., Chigrin, D.N., Lavrinenko, A.V., Torres, C.M.S.: Resonant add-drop filter based on a photonic quasicrystal. Opt. Express **13**(3), 826–835 (2005). https://doi.org/10.1364/OPEX.13.000826
7. Farmani, A., Mir, A., Irannejad, M.: 2D-FDTD simulation of ultra-compact multifunctional logic gates with nonlinear photonic crystal. J. Opt. Soc. Am. B **36**(4), 811 (2019). https://doi.org/10.1364/josab.36.000811
8. Rubio-Mercedes, C.E., Hernandez-Figueroa, H.E., Rodriguez-Esquerre, V.F., Davanco, M.: Finite-element frequency-domain analysis of 2D photonic crystal resonant cavities. In: Proceedings of the 4th International Conference on Numerical Simulation of Optoelectronic Devices, 2004. NUSOD '04., pp. 111–112 (2004). https://doi.org/10.1109/NUSOD.2004.1345181
9. Rodriguez-Esquerre, V.F., Koshiba, M., Hernandez-Figueroa, H.E.: Finite-element analysis of photonic crystal cavities: time and frequency domains. J. Lightwave Technol. **23**(3), 1514–1521 (2005). https://doi.org/10.1109/JLT.2005.843441
10. Gordon, D., Gordon, R.: CADD: a seamless solution to the domain decomposition problem of subdomain boundaries and cross-points. Wave Motion **98**, 102649–11 (2020). https://doi.org/10.1016/j.wavemoti.2020.102649
11. Gander, M.J., Santugini, K.: Cross-points in domain decomposition methods with a finite element discretization. Electron. Trans. Numer. Anal. **45**, 219–240 (2016)
12. North, E., Tsynkov, S., Turkel, E.: Non-iterative domain decomposition for the Helmholtz equation with strong material discontinuities. Appl. Numer. Math. **173**, 51–78 (2022). https://doi.org/10.1016/j.apnum.2021.10.024
13. Ryaben'kii, V.S.: Method of Difference Potentials and Its Applications. Springer Series in Computational Mathematics, vol. 30, p. 538. Springer, Berlin (2002). https://doi.org/10.1007/978-3-642-56344-7. Translated from the 2001 Russian original by Nikolai K. Kulman
14. Ryaben'kii, V.S., Tsynkov, S.V.: A Theoretical Introduction to Numerical Analysis, p. 537. Chapman & Hall/CRC, Boca Raton (2007)
15. Bayliss, A., Goldstein, C.I., Turkel, E.: On accuracy conditions for the numerical computation of waves. J. Comput. Phys. **59**(3), 396–404 (1985)
16. Babuška, I.M., Sauter, S.A.: Is the pollution effect of the FEM avoidable for the Helmholtz equation considering high wave numbers? SIAM Rev. **42**(3), 451–484 (2000). https://doi.org/10.1137/S0036142994269186. Reprint of SIAM J. Numer. Anal. 34 (1997), no. 6, 2392-2423 [MR1480387 (99b:65135)]
17. Sommerfeld, A.: Partial Differential Equations in Physics, p. 335. Academic Press, Inc., New York, N.Y. (1949). Translated by Ernst G. Straus
18. Engquist, B., Majda, A.: Absorbing boundary conditions for the numerical simulation of waves. Math. Comp. **31**(139), 629–651 (1977). https://doi.org/10.2307/2005997
19. Hagstrom, T., Hariharan, S.I.: Accurate boundary conditions for exterior problems in gas dynamics. Math. Comp. **51**(184), 581–597 (1988). https://doi.org/10.2307/2008764
20. Bayliss, A., Turkel, E.: Radiation boundary conditions for wave-like equations. Commun. Pure Appl. Math. **33**(6), 707–725 (1980). https://doi.org/10.1002/cpa.3160330603
21. Bayliss, A., Gunzburger, M., Turkel, E.: Boundary conditions for the numerical solution of elliptic equations in exterior regions. SIAM J. Appl. Math. **42**(2), 430–451 (1982). https://doi.org/10.1137/0142032
22. Tsynkov, S.V.: Numerical solution of problems on unbounded domains. A review. Appl. Numer. Math. **27**(4), 465–532 (1998). https://doi.org/10.1016/S0168-9274(98)00025-7
23. Bayliss, A., Goldstein, C.I., Turkel, E.: An iterative method for the Helmholtz equation. J. Comput. Phys. **49**(3), 443–457 (1983). https://doi.org/10.1016/0021-9991(83)90139-0
24. Deraemaeker, A., Babuška, I., Bouillard, P.: Dispersion and pollution of the FEM solution for the Helmholtz equation in one, two and three dimensions. Int. J. Numer. Meth. Eng. **46**(4), 471–499 (1999)
25. Harari, I., Turkel, E.: Accurate finite difference methods for time-harmonic wave propagation. J. Comput. Phys. **119**(2), 252–270 (1995). https://doi.org/10.1006/jcph.1995.1134
26. Singer, I., Turkel, E.: High-order finite difference methods for the Helmholtz equation. Comput. Methods Appl. Mech. Eng. **163**(1–4), 343–358 (1998). https://doi.org/10.1016/S0045-7825(98)00023-1
27. Turkel, E., Gordon, D., Gordon, R., Tsynkov, S.: Compact 2D and 3D sixth order schemes for the Helmholtz equation with variable wave number. J. Comput. Phys. **232**, 272–287 (2013). https://doi.org/10.1016/j.jcp.2012.08.016
28. Singer, I., Turkel, E.: Sixth-order accurate finite difference schemes for the Helmholtz equation. J. Comput. Acoust. **14**(3), 339–351 (2006). https://doi.org/10.1142/S0218396X06003050
29. Britt, S., Tsynkov, S., Turkel, E.: Numerical simulation of time-harmonic waves in inhomogeneous media using compact high order schemes. Commun. Comput. Phys. **9**(3), 520–541 (2011). https://doi.org/10.4208/cicp.091209.080410s
30. Reznik, A.A.: Approximation of surface potentials of elliptic operators by difference potentials. Soviet Math. Dokl. **25**(2), 543–545 (1982)
31. Medvinsky, M., Tsynkov, S., Turkel, E.: The method of difference potentials for the Helmholtz equation using compact high order schemes. J. Sci. Comput. **53**(1), 150–193 (2012). https://doi.org/10.1007/s10915-012-9602-y
32. Medvinsky, M., Tsynkov, S., Turkel, E.: High order numerical simulation of the transmission and scattering of waves using the method of difference potentials. J. Comput. Phys. **243**, 305–322 (2013). https://doi.org/10.1016/j.jcp.2013.03.014
33. Medvinsky, M., Tsynkov, S., Turkel, E.: Solving the Helmholtz equation for general smooth geometry using simple grids. Wave Motion **62**, 75–97 (2016). https://doi.org/10.1016/j.wavemoti.2015.12.004

34. Albright, J., Epshteyn, Y., Medvinsky, M., Xia, Q.: High-order numerical schemes based on difference potentials for 2D elliptic problems with material interfaces. Appl. Numer. Math. **111**, 64–91 (2017). https://doi.org/10.1016/j.apnum.2016.08.017
35. Britt, D.S., Tsynkov, S.V., Turkel, E.: A high-order numerical method for the Helmholtz equation with nonstandard boundary conditions. SIAM J. Sci. Comput. **35**(5), 2255–2292 (2013). https://doi.org/10.1137/120902689
36. Reznik, A.A.: Approximation of the surface potentials of elliptic operators by difference potentials and solution of boundary-value problems (in Russian). PhD thesis, Moscow Institute of Physics and Technology, Moscow (1983)
37. Karageorghis, A.: A note on the Chebyshev coefficients of the general order derivative of an infinitely differentiable function. J. Comput. Appl. Math. **21**(1), 129–132 (1988). https://doi.org/10.1016/0377-0427(88)90396-2
38. Hesthaven, J.S., Gottlieb, S., Gottlieb, D.: Spectral Methods for Time-Dependent Problems. Cambridge Monographs on Applied and Computational Mathematics, vol. 21, p. 273. Cambridge University Press, Cambridge (2007). https://doi.org/10.1017/CBO9780511618352
39. Talebi, N., Mahjoubfar, A., Shahabadi, M.: Plasmonic ring resonator. J. Opt. Soc. Am. B **25**(12), 2116–2122 (2008). https://doi.org/10.1364/JOSAB.25.002116
40. Wu, C.-T., Huang, C.-C., Lee, Y.-C.: Plasmonic wavelength demultiplexer with a ring resonator using high-order resonant modes. Appl. Opt. **56**(14), 4039–4044 (2017). https://doi.org/10.1364/AO.56.004039
41. Araújo C., J.C., Engström, C.: On spurious solutions encountered in Helmholtz scattering resonance computations in $\mathbb{R}^d$ with applications to nano-photonics and acoustics. J. Comput. Phys. 429, 110024–20 (2021). https://doi.org/10.1016/j.jcp.2020.110024
42. Petropavlovsky, S., Tsynkov, S., Turkel, E.: 3D time-dependent scattering about complex shapes using high order difference potentials. J. Comput. Phys. **471**, 111632 (2022). https://doi.org/10.1016/j.jcp.2022.111632